Clinopyroxene–liquid equilibria and geothermobarometry in natural and experimental tholeiites

DOI:
10.1093/petrology/egz042

Document Version
Accepted author manuscript

Draft Manuscript for Review

Clinopyroxene–liquid equilibria and geothermobarometry in natural and experimental tholeiites: the 2014–2015 Holuhraun eruption, Iceland

Journal:	*Journal of Petrology*
Manuscript ID	JPET-Nov-18-0152.R2
Manuscript Type:	Original Manuscript
Date Submitted by the Author:	n/a
Complete List of Authors:	Neave, David; Leibniz Universität Hannover, Institut für Mineralogie; The University of Manchester, School of Earth and Environmental Sciences Bali, Eniko; Haskoli Islands, Institute of Earth Sciences, NordVulk Guðfinnsson, Guðmundur ; Haskoli Islands, Institute of Earth Sciences, NordVulk Halldórsson, Saemundur; Haskoli Islands, Institute of Earth Sciences, NordVulk Kahl, Maren; Haskoli Islands, Institute of Earth Sciences; Ruprecht Karls Universität Heidelberg, Institut für Geowissenschaften Schmidt, André-Sebastian; Leibniz Universität Hannover, Institut für Mineralogie Holtz, François; University of Hannover, Institute of Mineralogy
Keyword:	geothermobarometry, clinopyroxene, tholeiite, experimental petrology, Iceland

Clinopyroxene–liquid equilibria and geothermobarometry in natural and experimental tholeiites: the 2014–2015 Holuhraun eruption, Iceland

David A. Neave[1,2]*, Enikő Bali[3], Guðmundur H. Guðfinnsson[3], Sæmundur A. Halldórsson[3], Maren Kahl[3,4], André-Sebastian Schmidt[1] and François Holtz[1]

[1]Leibniz Universität Hannover, Institut für Mineralogie, Callinstraße 3, 30167 Hannover, Germany

[2]School of Earth and Environmental Sciences, The University of Manchester, Oxford Road, Manchester, M13 9PL, United Kingdom

[3]NordVulk, Institute of Earth Sciences, University of Iceland, Askja, Sturlugata 7, 101 Reykjavík, Iceland

[4] Institut für Geowissenschaften, Ruprecht-Karls-Universität Heidelberg, Im Neuenheimer Feld 234–236, 69120 Heidelberg, Germany

*Corresponding author: david.neave@manchester.ac.uk

Revised manuscript for second resubmission to *Journal of Petrology*

July 2019

Abstract: 514 words. Main text: 11009 words

Running title: Clinopyroxene in tholeiitic magmas

ABSTRACT

Clinopyroxene–liquid geothermobarometry is a widely used tool for estimating the conditions under which mafic magmas are stored before they erupt. However, redox variability, sector zoning and disequilibrium crystallisation present major challenges to the robust estimation of magma storage conditions. Moreover, most recent studies seeking to address these challenges have focused on clinopyroxenes from alkalic systems and are thus of limited use for understanding clinopyroxenes from the tholeiitic systems that dominate global magma budgets. Here we combine observations on natural clinopyroxenes from the 2014–2015 Holuhraun lava in Iceland with observations on experimental clinopyroxenes synthesised during high-pressure, high-temperature experiments on the same lava in order to investigate clinopyroxene–liquid equilibria in tholeiitic systems and optimising geothermobarometric strategies. Natural clinopyroxenes from the 2014–2015 Holuhraun lava are sector zoned, with $\{\bar{1}11\}$ hourglass sectors being enriched in enstatite-ferrosillite component at the expense of all other components with respect to $\{hk0\}$ prism sectors. In contrast with observations on clinopyroxenes from alkalic systems, sector zoning in clinopyroxenes from the 2014–2015 Holuhraun lava is characterised by differences in Ca and Na contents as well as in Ti and Al contents. The products of crystallisation experiments performed at 100–600 MPa and 1140–1220 °C on a powdered starting glass at two suites of melt H_2O content–oxygen fugacity conditions (~0.1 wt.% H_2O and close to the graphite–oxygen redox buffer, and 0.5–1.0 wt.% H_2O and approximately one and half log units above the quartz–fayalite–magnetite redox buffer) demonstrate that clinopyroxene crystals from nominally equilibrium experiments can preserve strongly disequilibrium compositions. The compositional systematics of experimental clinopyroxenes are consistent with the presence of sector zoning. Furthermore, the magnitude of compositional variability increases with decreasing melt H_2O contents and increasing deviations of experimental temperatures below clinopyroxene liquidus

temperatures (i.e. degrees of undercooling *sensu lato*), indicating that kinetic processes play a key role in controlling clinopyroxene compositions under even notionally equilibrium conditions. Few published analyses of experimental clinopyroxene crystals may thus represent truly equilibrium compositions. Stoichiometric calculations on natural and experimental clinopyroxenes show that Fe^{3+} is a major constituent of clinopyroxenes from tholeiitic magmas under naturally relevant oxygen fugacity conditions. They also show that Fe^{3+} is most likely incorporated as Ca- and Al- bearing Ca-Fe-Tschermak's component rather than Na-bearing aegirine component at oxygen fugacities up to one and half log units above the quartz–fayalite–magnetite buffer. Elevated oxygen fugacities are thus less likely to compromise clinopyroxene–liquid geothermobarometry than previously thought. Guided by our experimental results, we combined published descriptions of clinopyroxene–liquid equilibria with geothermobarometric equations to develop an internally consistent and widely applicable method for performing geothermobarometry on tholeiitic magmas that does not require equilibrium zones to be selected *a priori*. Applying this method to natural clinopyroxene crystals from the 2014–2015 Holuhraun lava that formed under low but variable degrees of undercooling (perhaps 25 °C or less) returns values in excellent agreement with those from independent methods (232±86 MPa, 1161±11 °C). Robust estimates of magma storage conditions can thus be obtained by performing clinopyroxene–liquid geothermobarometry on tholeiitic magmas when disequilibrium is suitably accounted for.

Key words: geothermobarometry; clinopyroxene; tholeiite; experimental petrology; Iceland

INTRODUCTION

Clinopyroxene is a key constituent of many mantle, igneous and metamorphic rocks. Its stability across diverse pressure–temperature–composition (*P–T–X*) conditions derives from its ability to incorporate a large range of cations in both octahedral and tetrahedral coordination states (Morimoto *et al.*, 1988). Although this compositional plasticity makes it challenging to model clinopyroxene chemistry (e.g., Sack and Ghiorso, 1994; Green *et al.*, 2012), it does mean that clinopyroxene can record more information about the conditions under which it formed than chemically simpler minerals such as olivine (e.g., Putirka, 2008). For example, the *P*-sensitive incorporation of Na into clinopyroxene can be exploited as a geobarometer for estimating the depths at which volcanic products were stored prior to eruption (Putirka *et al.*, 1996). Such depth estimates are vital for reconstructing magmatic plumbing system architectures and hence understanding mechanisms of crustal accretion (e.g., Maclennan *et al.*, 2001) and interpreting geophysical signals of magma movement before and during volcanic eruptions (e.g., Longpré *et al.*, 2014). However, obtaining reliable values from clinopyroxene geobarometers is not always straightforward: variations in oxygen fugacity (fO_2), sector zone development, disequilibrium crystallisation and uncertainties in geobarometric equations can all lead to spurious results, even when geochemical analyses are of superior quality (Mollo *et al.*, 2013; Hammer *et al.*, 2016; Neave and Putirka, 2017). Here we use observations on natural clinopyroxenes from an archetypal tholeiitic basalt emplaced during the 2014–2015 Holuhraun eruption in Iceland to identify sources of uncertainty in magma storage depth estimates. Observations on natural samples are complemented by experimental observations designed to test the reliability of Neave and Putirka's (2017) clinopyroxene–liquid geobarometer and facilitate the optimisation of methods for determining the conditions under which the tholeiitic magmas that dominate global magma budgets crystallise.

Clinopyroxene in mafic magmas

Tholeiitic basalts erupt at mid-ocean ridges, many ocean islands and some volcanic arcs. They are typically characterised by the presence of olivine, plagioclase and augitic clinopyroxene (e.g., Bryan, 1983; Tormey *et al.*, 1987), though low-Ca pyroxene (pigeonite or orthopyroxene) may also occur (e.g., Lindsley, 1983; Grove and Juster, 1989). Although augite compositions can be summarised with reference to the pyroxene quadrilateral bounded by the diopside–hedenbergite (Di–Hd; $CaMgSi_2O_6$–$CaFe^{2+}Si_2O_6$) and enstatite–ferrosillite (En–Fs; $Mg_2Si_2O_6$–$Fe^{2+}{}_2Si_2O_6$) solid solutions, natural crystals often contain appreciable quantities of Ti, Al, Cr, Fe^{3+} and Na in non-quadrilateral components such as Ca-Tschermak's component (CaTs; $CaAlAlSiO_6$). The *P*-dependent incorporation of Na into clinopyroxene as jadeite component (Jd; $NaAlSi_2O_6$) is of particular petrological interest because of its use in Jd-in-clinopyroxene geobarometery (e.g., Putirka *et al.*, 1996). However, the incorporation of aegirine component (Ae; $NaFe^{3+}Si_2O_6$) alongside Jd component under oxidising conditions can complicate relationships between *P* and clinopyroxene Na contents (Blundy *et al.*, 1995), potentially limiting the reliability of Jd-in-clinopyroxene geobarometry when magma Fe^{3+} contents are high (Neave and Putirka, 2017). Although Mössbauer spectroscopy on basanite-hosted clinopyroxenes from the Canary Islands confirms that clinopyroxenes in oxidised ocean-island magmas can contain significant quantities of Fe^{3+} ($Fe^{3+}/\Sigma Fe \sim 0.37$–$0.51$; Weis *et al.*, 2015), a paucity of comparable data from more reduced magmas and the products of experiments performed at controlled fO_2 conditions means that the effects of magma redox state on the performance of Jd-in-clinopyroxene geobarometry remain largely unquantified. By carrying out experiments at two different redox conditions, we aim to start exploring the effects of fO_2 on augite chemistry and clinopyroxene–liquid geothermobarometry; a comprehensive assessment is however beyond the scope of this study.

Observations from natural and experimental clinopyroxenes

Augitic clinopyroxenes often exhibit sector zoning that manifests as compositional variability between families of crystallographically related sectors (Strong, 1969; Hollister and Gancarz, 1971; Downes, 1974; Dowty, 1976; Skulski *et al.*, 1994; Ubide *et al.*, 2019). Chemical differences between sectors reflect the ability of different crystal faces to incorporate cations in equilibrium proportions during crystal growth (Nakamura, 1973; Leung, 1974; Dowty, 1976). For example, Nakamura and Coombs (1973) observed that {100} sectors of augite crystals from the tholeiitic Tawhiroko intrusion in New Zealand are characterised by disequilibrium componentry, with En and Fs components being enriched at the expense of Di and Hd components when compared with {010} and {110} sectors from the same grains. However, the sense and magnitude of sector zoning depends strongly on the degree of undercooling (i.e. the difference between the liquidus *T* and the magmatic or experimental *T* at which crystallisation occurs) experienced (Kouchi *et al.*, 1983). Thus, simply assuming that low-EnFs (i.e. Ti-, Al- and Na-rich) sectors record equilibrium growth conditions may be inappropriate. For instance, in their recent study of ankaramites from Haleakalā, Hawaii, Welsch *et al.* (2016) described complex sector zoning resulting from the rapid, dendritic crystallisation of Ti-, Al- and Na-rich {$\bar{1}11$} hourglass sectors at high degrees of undercooling followed by the subsequent infilling of Ti-, Al- and Na-poor {$hk0$} prism sectors at lower degrees of undercooling. In this case, {$hk0$} sectors were interpreted as recording equilibrium growth conditions and hence thought to yield reliable geobarometric results (Hammer *et al.*, 2016). However, despite Welsch *et al.* (2016) and Hammer *et al.* (2016) making compelling cases for critically investigating how sector zoning influences crystal compositions and geothermobarometric calculations, it is currently unclear whether their observations on alkalic systems provide a reliable framework for interpreting data from tholeiitic systems (Neave and Putirka, 2017; Ubide *et al.*, 2019).

Although the degree of undercooling mediates the nature and degree of sector zone development during crystallisation (Kouchi *et al.*, 1983; Welsch *et al.*, 2016), it also affects the composition of crystals independently of sector zone development (Lofgren *et al.*, 2006; Mollo and Hammer, 2017). That is, clinopyroxene bulk compositions depend on the degree of undercooling as well as on the prevailing *P–T–X* conditions. Augite crystals formed at high undercooling are characterised by an excess of non-quadrilateral components (Lofgren *et al.*, 2006; Mollo and Hammer, 2017), potentially resulting in the calculation of spurious storage conditions by clinopyroxene–liquid geothermobarometry, as demonstrated in dynamic crystallisation experiments with high cooling rates (Mollo *et al.*, 2010). Filtering clinopyroxenes for multicomponent equilibrium nevertheless provides a way to exclude disequilibrium compositions from geothermobarometric calculations (e.g., Mollo *et al.*, 2013) and has enabled the calculation of coherent magma storage depths in a number of settings including Iceland (e.g., Halldórsson *et al.*, 2018). However, such multicomponent filtering has yet to be validated with experiments on tholeiitic compositions – much of the work carried out to date has focussed on alkali basalts from Mt. Etna, Italy (e.g., Mollo *et al.*, 2011, 2013, 2018). We thus aim to develop an experimentally validated strategy for robustly identifying equilibrium clinopyroxene–liquid pairs in tholeiitic magmas that will be of widespread use for studying systems beyond the 2014–2015 Holuhraun lava.

The 2014–2015 Holuhraun eruption

The 2014–2015 Holuhraun volcano-tectonic event in central Iceland was one of the best monitored basaltic fissure eruptions ever to have taken place (Sigmundsson *et al.*, 2015; Ágústsdóttir *et al.*, 2016; Guðmundsson *et al.*, 2016). Approximately 1.2 km^3 of lava (dense rock equivalent) was emplaced on the Dyngjusandur plain north of the Vatnajökull icecap over the course of the eight-month long eruption (Fig. 1; Pedersen *et al.*, 2017; Bonny *et al.*, 2018), making it the volumetrically largest eruption in Europe since the 1783–1784 Laki

Fires (Thordarson and Self, 1993). Subsidence within the Bárðarbunga caldera was recorded from the onset of dyke intrusion (Sigmundsson *et al.*, 2015), and continued at a rate commensurate with the decaying mass flux at the vent until the end of the eruption (Guðmundsson *et al.*, 2016). A magmatic connection between the vent and a steadily deflating reservoir beneath the Bárðarbunga caldera thus appears to have been maintained throughout the course of the eruption. Geodetic observations place a putative source reservoir at a depth of 8–12 km beneath the Bárðarbunga central volcano (Guðmundsson *et al.*, 2016), consistent with depths from carefully implemented – if not experimentally verified – petrological geobarometry based on clinopyroxene–liquid geothermobarometry, olivine–plagioclase–augite–melt (OPAM) thermal minima positions and melt and fluid inclusion entrapment pressures (Bali *et al.*, 2018; Halldórsson *et al.*, 2018; Hartley *et al.*, 2018).

The 2014–2015 Holuhraun lava is a moderately evolved and strikingly homogenous tholeiite similar in composition to magmas erupted across Iceland and the mid-ocean ridge system more broadly (Halldórsson *et al.*, 2018). Crystals of olivine, plagioclase and augitic clinopyroxene were erupted throughout but are present in sufficiently low abundances (≤5 vol.%) that some whole-rock compositions approximate those of magmatic liquids; whole-rock compositions overlap with melt inclusion compositions (Hartley *et al.*, 2018). The presence of clinopyroxene in an otherwise modestly porphyritic basalt makes the 2014–2015 Holuhraun lava an ideal subject for evaluating clinopyroxene geothermobarometry in tholeiitic systems because most clinopyroxene crystals are likely to have grown from liquids directly parental to their carrier melts (i.e. whole-rock ≈ carrier liquid + equilibrium crystal assemblage); note that this is not the case for some primitive olivine and plagioclase compositions (Halldórsson *et al.*, 2018). Crystal-poor whole-rock samples can thus be used as starting materials for experiments designed to mimic the final stages of magmatic evolution. Here we focus on poorly porphyritic MSR161014 (≤5 vol.% macrocrysts; Halldórsson *et al.*,

2018) from the main phase of the 2014–2015 Holuhraun eruption. This sample was collected on day 50 of the eruption at 64.902° N, 16.686° W by the 2014–2015 Holuhraun Eruption Team of the University of Iceland (Fig. 1). It has been thoroughly characterised geochemically and is thus well-suited to the focussed investigation we present here.

METHODS

Experimental methods

A starting glass powder for high-*P*, high-*T* experiments was produced by fusing 10 g of powder from sample MSR161014 in a muffle furnace at the Institut für Mineralogie of the Leibniz Universität Hannover, Germany. By using a quenched glass powder we sought to minimise reactions prior to crystallising an equilibrium assemblage in order to mimic crystallisation from superliquidus conditions (Mollo and Hammer, 2017). The MSR161014 powder was melted at 1600 °C in a large-volume Pt crucible under air to prevent Fe loss. A homogenous glass powder was then obtained by quenching the crucible in H_2O after 1 hour and grinding the resulting glass chips in an agate disc mill. The resulting glass powder was then melted, quenched and ground a second time prior to storage in a desiccator. The starting glass powder's composition is within analytical uncertainty of published whole-rock compositions for MSR161014 (Supplementary Material; Halldórsson *et al.*, 2018).

High-*P*, high-*T* experiments were carried out under different fO_2 conditions by using different capsule designs. Experimental redox conditions close to (or below) CCO (i.e. at or below ~QFM−1.7) and QFM+1 were chosen to bracket those recorded in the 2014–2015 Holuhraun lava (maximum fO_2 ~ QFM+0.5; Bali *et al.*, 2018). Reducing conditions were achieved by loading ~20 mg of dried starting glass powder into graphite inner capsules that were then enclosed within Pt outer capsules. In this case, the graphite inner capsules theoretically buffered experimental samples at an fO_2 at or below the graphite–oxygen (CCO)

redox buffer, with excess O_2 reacting to form CO_2 (Holloway *et al.*, 1992; Jakobsson and Óskarsson, 1994; Médard *et al.*, 2008). In a second suite of capsules designed to run under moderately oxidising conditions, ~60 mg of dried starting glass powder was loaded into $Au_{80}Pd_{20}$ (AuPd) capsules that had been pre-saturated with ~0.2 wt.% Fe (e.g., Gaetani and Grove, 1998; Balta *et al.*, 2011). With the intention of buffering samples at an fO_2 approximately one log unit above the quartz–fayalite–magnetite (QFM) redox buffer, no H_2O was added (e.g., Husen *et al.*, 2016). Small quantities of H_2O (~0.5 wt.%) were nevertheless expected to form by the reaction of trace H_2 in the pressure medium with O_2 liberated from the reduction Fe_2O_3 in the starting glass (Botcharnikov *et al.*, 2005; Husen *et al.*, 2016).

Experimental runs were performed by suspending either graphite-Pt double capsules or AuPd capsules from thin Pt wires in the hot zone of an internally heated pressure vessel (IHPV) at the Institut für Mineralogie of the Leibniz Universität Hannover, Germany (e.g., Berndt *et al.*, 2002). Experiments were performed at 100, 300 and 600 MPa using an Ar pressure medium; no 600-MPa experiments were performed using graphite-Pt double capsules. Pressure was continuously monitored with a strain gauge manometer and did not vary more than the measurement uncertainty (5 MPa) during experimental runs. Experiments were performed at 1140, 1160 and 1180 °C for all *P* conditions in order to bracket magma storage conditions estimated in earlier work (Halldórsson *et al.*, 2018); additional higher-*T* experiments were performed at 1200 and 1220 °C for some *P*–fO_2 combinations (Table 1). Experimental samples were heated to 20 °C below the target *T* at a rate of 50 °C/min, and then to the target *T* at a rate of 10 °C/min in order to avoid overshooting; no high-*T* treatments were applied at the start of any runs. After holding samples at the target *T* for one hour, thermal oscillations of ±10 °C were imposed for the first third of each experimental run to promote the formation of large crystals and large melt pools (Erdmann and Koepke, 2016). Temperature was monitored across the vessel's 25 mm-tall hot zone with four unsheathed S-

type (Pt-$Pt_{90}Rh_{10}$) thermocouples and was typically within 5 °C of the target temperature (no measured temperature deviated more than 10 °C from the target temperature). Run durations varied from 48 hours for the hottest experiments to 96–120 hours for the coolest. Capsules were quenched rapidly at the end of each run by fusing the Pt wires on which they were suspended, dropping them into a cold zone at vessel's base.

Analytical methods

After capsules had been weighed to validate their integrity during high-*P*, high-*T* runs, experimental samples (including capsule pieces) were mounted in epoxy resin and polished for imaging and microanalysis. Sample pieces from superliquidus experiments were mounted in epoxy resin and double-polished for spectroscopic analyses to monitor experimental H_2O contents. Further samples fragments from superliquidus experiments were conserved for determining glass $Fe^{3+}/\Sigma Fe$ values by colorimetry to monitor experimental fO_2 conditions. Natural clinopyroxenes were investigated in a polished thin section cut from a block of MSR161014.

Both natural and experimental samples were imaged using a JEOL JSM-7610F field emission gun scanning electron microscope (FEG-SEM) at the Institut für Mineralogie of the Leibniz Universität Hannover, Germany. Glass, mineral and AuPd-capsule compositions were determined by electron probe microanalysis (EPMA) at the Institut für Mineralogie of the Leibniz Universität Hannover, Germany using a Cameca SX100 instrument. Silicon, Ti, Al, Cr, Fe, Mn, Mg, Ca, Na, K and P were measured in glasses with a beam size of 12 μm, an accelerating voltage of 15 kV and a current of 10 nA. Silicon, Ti, Al, Cr, Fe, Mn, Mg, Ca, Na and K were measured in minerals with a beam size of 1 μm, an accelerating voltage of 15 kV and a current of 15 nA. Gold, Pd and Fe were measured in capsules with a beam size of 1 μm, an accelerating voltage of 15 kV and a current of 40 nA. Elements were counted on peak for 20 s, with the exceptions of Si and Na that were counted on peak for 10 s to minimise drift

and migration respectively. Background counting times were half on-peak counting times. The following standards were used for calibration: wollastonite (Si and Ca), TiO_2 (Ti), jadeite (Al), Cr_2O_3 (Cr), Fe_2O_3 (for Fe in silicates), Fe metal (for Fe in capsules), Mn_3O_4 (Mn), MgO (Mg), albite (Na), orthoclase (K), apatite (P), Au metal (Au) and Pd metal (Pd).

To ensure consistency across multiple analytical sessions, analyses of unknowns were normalised to secondary standards as follows: glass analyses were normalised to VG-2 basaltic glass (NMNH 111240-52; using the preferred MgO content); clinopyroxene and plagioclase analyses were normalised to Kakanui augite (NMNH 122142; using preferred values); olivine analyses were normalised to San Carlos olivine (NMNH 111312-44) (Jarosewich *et al.*, 1980). Accuracy and precision were monitored by measuring the following additional secondary standards: A-99 basaltic glass (NMNH 113498), Ney County Cr-augite (NMNH 164905) and Lake County plagioclase (NMNH 115900) (Jarosewich *et al.*, 1980, 1987). Major (>1 wt.%) and minor (<1 wt.%) elements were typically determined with accuracies better than 2% and 10%, and 1σ precisions better than 2% and 15% respectively. Typical standard analyses are provided alongside analyses of our experimental products in the Supplementary Material.

Water contents of superliquidus experiments were determined by Fourier-transform infrared (FTIR) spectroscopy using a Bruker IFS88 instrument at the Institut für Mineralogie of the Leibniz Universität Hannover, Germany, and an absorption coefficient for the 3500 cm^{-1} H_2O_t band given by Shishkina *et al.* (2010). The speciation of iron (i.e. $Fe^{3+}/\Sigma Fe$) in superliquidus experiments was determined by colorimetric analysis following the methods of Schuessler *et al.* (2008). The accuracy of precision of $Fe^{3+}/\Sigma Fe$ determinations were monitored by measuring an in-house andesite standard (PU-3; Borisov *et al.*, 2018). Superliquidus glass H_2O contents and $Fe^{3+}/\Sigma Fe$ values are provided in Table 1.

PETROGRAPHIC RESULTS

Natural samples

MSR161014 is a fresh, poorly porphyritic basalt (≤5 vol.% macrocrysts) containing, in order of abundance, plagioclase, clinopyroxene and olivine macrocrysts in a crystalline groundmass (Fig. 2). Note that we simply define macrocrysts as crystals that are >100 μm in length and texturally distinct from the groundmass (e.g., Thomson and Maclennan, 2013). Plagioclase and clinopyroxene macrocrysts are typically 100–400 μm in length while olivine macrocrysts are slightly smaller, with lengths of 100–200 μm. Macrocrysts occur as individual grains and within glomerocrystic clusters. Clinopyroxenes and plagioclase macrocrysts frequently occur in subophitic arrangement, though monomineralic glomerocrysts of plagioclase and clinopyroxene are also present. There are no clear textural differences between isolated macrocrysts and macrocrysts in glomerocrysts. Concentric and sector zoning textures are evident in plagioclase and clinopyroxene respectively when viewed under crossed polars. (Fig. 2b). Fe-Ti oxides are restricted to the groundmass.

Backscattered electron (BSE) imaging reveals that clinopyroxene macrocrysts cores are generally equant, sub- to euhedral and enveloped by complex rims intergrown with the sample's crystalline groundmass (Fig. 3). Two compositionally distinct families of sector zones can be identified on the basis of their different BSE intensities. Combining SEM observations with optical microscopy indicates that low BSE intensities are associated with $\{\bar{1}11\}$ hourglass sectors. For example, the macrocryst shown in Fig. 3a (cpx-21) has been cut parallel to (010) such that [100] and [001] lie within the plane of the thin section and are separated by a β-angle of ~105°. High-BSE-intensity sectors in this image thus formed by growth on cleavage-parallel {110} faces, and low-BSE-intensity sectors by growth on cleavage-oblique $\{\bar{1}11\}$ faces (e.g., Downes, 1974). A small high-BSE-intensity zone associated with growth on {010} faces is visible in the centre of the macrocryst. In contrast, the macrocryst shown in Fig. 3b (cpx-22) has been cut between (100) and (001) such that

only [010] lies close to the plane of the thin section. Low-BSE-intensity sectors in this macrocryst are still associated with growth on $\{\bar{1}11\}$ faces; high-BSE-intensity sectors reflect growth on $\{110\}$ and $\{010\}$ faces. However, the plane of the thin section must lie close to the interface between $\{\bar{1}11\}$ and $\{100\}$ sectors because (111) and $(\bar{1}11)$ faces cannot be distinguished from each other (Leung, 1974; Welsch *et al.*, 2016). Further macrocrysts in the sample were cut close to (001), confirming the association of high BSE intensities with $\{100\}$, $\{010\}$ and $\{110\}$ prism sectors (Supplementary Material).

Concentric zoning is present in all of the clinopyroxene macrocrysts imaged (Fig. 3). Although variations in BSE intensity associated with concentric zoning are comparable with those associated with sector zoning, there are, with the exception of very high-BSE-intensity rims in contact with the groundmass, no consistent changes in BSE intensity along core-to-rim profiles. Importantly, concentric zones can be traced across sector zone boundaries, indicating that all sectors grew concurrently (cf. Welsch *et al.*, 2016).

Experimental samples

Experimental conditions are summarised in Table 1 and BSE images of typical experimental products are shown in Fig 4. Crystals are typically 10–40 μm but occasionally up to 200 μm in length and are separated by pools of quenched and visually homogenous glass. Most crystals are euhedral; only olivine crystals show consistently rounded morphologies. No compositional zonation was observed in experimental olivine and plagioclase compositions. Although the texture of experimental clinopyroxene crystals varies considerably between the products of different experiments, two overarching trends can nevertheless be identified. Firstly, the largest clinopyroxene crystals grew in high-T, high-melt-fraction (high-F) experiments (Figs. 4a and 4c). Specifically, large (>20 μm diameter) clinopyroxene crystals only grew in the highest-T subliquidus experiments performed under any combination of P and fO_2 conditions. Some large clinopyroxenes also show evidence for internal zonation that

is reminiscent of the complex zoning observed in natural crystals (Figs. 4a and 4d). No large clinopyroxene crystals were produced in our 600-MPa experiments, though we did not bracket the liquidus under these conditions (Fig. 4b). Secondly, clinopyroxene crystals in low-T, low-F experiments typically form chains of small (<10 μm diameter), intergrown grains (Fig. 4d).

MICROANALYTICAL RESULTS

Natural samples

The composition of the experimental starting glass prepared from sample MSR161014 is shown in Fig. 5 (black star) and is comparable with published whole-rock analyses of this sample (Halldórsson *et al.*, 2018). MSR161014 is slightly more primitive (6.82 wt.% MgO) than matrix glass samples collected during the eruption (5.34–6.74 wt.% MgO; Halldórsson *et al.*, 2018) and is instead most similar to the composition of evolved melt inclusions (Hartley *et al.*, 2018), consistent with its slightly primitive and porphyritic nature (Fig. 2). Note that published matrix glasses with <6 wt.% MgO record syn-emplacement crystallisation and are unrepresentative of magmatic liquids at depth (Halldórsson *et al.*, 2018).

Olivine and plagioclase macrocryst compositions from MSR161014 are compared with published crystal compositions in Fig. 6 (Halldórsson *et al.*, 2018). Olivine macrocryst cores have similar forsterite contents [$X_{Fo} \sim 0.76$, where X_{Fo} = Mg/(Mg+Fe*) on a molar basis and all Fe is assumed to be Fe^{2+} (i.e. Fe*)] to the mode of published data ($X_{Fo} \sim 0.77$; Fig. 6a). Olivine rim compositions extend to lower X_{Fo} values than previously reported ($X_{Fo} \sim 0.62$ versus $X_{Fo} \sim 0.70$), probably because MSR161014 records an interval of crystallisation during lava flow emplacement. Most plagioclase macrocryst cores have similar anorthite contents [$X_{An} \sim 0.70$, where X_{An} = Ca/(Ca+Na+K) on a molar basis] to previously reported microcryst

and evolved macrocryst cores. Some macrocrysts have high-anorthite cores (X_{An} ~ 0.81), as observed in other samples (Halldórsson *et al.*, 2018; Hartley *et al.*, 2018). Plagioclase rims in MSR161014 also extend to more evolved compositions than previously reported (X_{An} ~ 0.58 versus X_{An} ~ 0.63).

Clinopyroxene macrocryst compositions are summarised in Fig. 7. Macrocrysts from MSR161014 are compositionally similar to the main macrocryst population observed in lavas emplaced throughout the eruption (Halldórsson *et al.*, 2018). Specifically, clinopyroxene macrocryst cores have Mg numbers [$Mg\#_{cpx}$, where $Mg\#_{cpx} = Mg/(Mg+Fe^*)$ on a molar basis and all Fe is assumed to be Fe^{2+} (i.e. Fe*)] in the range 0.75–0.82 (Fig.7a); a few rim analyses extend to $Mg\#_{cpx} < 0.75$. We did not observe any of the Cr-rich, high-$Mg\#_{cpx}$ compositions reported previously by Halldórsson *et al.* (2018). Despite exhibiting only modest variability in $Mg\#_{cpx}$, clinopyroxenes show considerable correlated variability in TiO_2 and Al_2O_3 (Fig. 7b): high- and low-TiO_2 (and Al_2O_3) populations with approximately >0.5 and <0.5 wt.% TiO_2 respectively can be identified at broadly consistent $Mg\#_{cpx}$ values.

Variability in clinopyroxene major element contents is illustrated in Fig.8. Most clinopyroxene analyses from MSR161014 define a population characterised by low Mg but high Ti, Al, Ca and Na contents. Chromium contents are also somewhat elevated in this low-Mg population. A subordinate population of analyses form a tail to distinctly higher Mg contents. These high-Mg analyses are also characterised by low Ti, Al, Ca and Na contents. Integrating spatial information from imaging with compositional information from EPMA on grains cpx-21 and cpx-22 demonstrates that low- and high-Mg analyses are located systematically within high- and low-BSE-intensity sectors respectively (Figs. 3 and 8). Namely, high-Mg analyses are from $\{\bar{1}11\}$ hourglass sectors, and low-Mg analyses from $\{100\}$, $\{010\}$ and $\{110\}$ (i.e. $\{hk0\}$) prism sectors.

Transects through high-BSE-intensity sectors are characterised by lower $Mg\#_{cpx}$ contents than transects though low-BSE-intensity sectors (Figs. 8 and 9). Importantly, transects from pairs of $\{hk0\}$ and $\{\bar{1}11\}$ sectors show correlated variations in $Mg\#_{cpx}$, indicating that they grew concurrently. When clinopyroxene compositions are converted into clinopyroxene components following Putirka (2008), it becomes clear that low-BSE-intensity $\{\bar{1}11\}$ hourglass sectors are considerably depleted in DiHd and CaTs components with respect to high-BSE-intensity $\{hk0\}$ prism sectors zones. Jadeite component contents are also generally lower in $\{\bar{1}11\}$ sectors. This sense of compositional variability shares some similarities with recently described variability in Etnean clinopyroxenes that can be expressed in terms of exchange between $\{hk0\}$ and $\{\bar{1}11\}$ sectors (Ubide *et al.*, 2019):

$$\left[\mathrm{Si}^{4+} + \mathrm{Fe}^{2+} + \mathrm{Mg}^{2+}\right]_{\{\bar{1}11\}} \rightleftharpoons \left[\mathrm{Ti}^{4+} + \mathrm{Al}^{3+} + \mathrm{Fe}^{3+}\right]_{\{hk0\}}. \quad (1)$$

Moreover, the incorporation of Na and Ti into the $\{hk0\}$ sectors is consistent with high CaTs component contents facilitating complex coupled substitutions (Bennett *et al.*, 2004):

$$\mathrm{Na}^{+} + \mathrm{Ti}^{4+} + \mathrm{CaAlAlSiO_6} \rightleftharpoons \mathrm{Ca}^{2+} + \mathrm{Al}^{3+} + \mathrm{NaTiAlSiO_6}. \quad (2)$$

However, we note that clinopyroxenes from the tholeiitic 2014–2015 Holuhraun lava also differ from those described in recent contributions on alkalic systems (cf. Welsch *et al.*, 2016; Ubide *et al.*, 2019). Specifically, sector zoning is well developed in Ca as well as in Ti, Al and Na such that $\{\bar{1}11\}$ hourglass sectors are not only depleted in non-quadrilateral components but in DiHd component as well. In other words, $\{\bar{1}11\}$ hourglass sectors appear to be enriched in EnFs component at the expense of all other components. In line with previous observations (Nakamura, 1973; Neave and Putirka, 2017), we propose that clinopyroxene sector zoning in tholeiitic systems can thus be generalised using a modified version of equation (1):

$$\left[\mathrm{Si}^{4+} + \mathrm{Fe}^{2+} + \mathrm{Mg}^{2+}\right]_{\{\bar{1}11\}} \rightleftharpoons \left[\mathrm{Ti}^{4+} + \mathrm{Al}^{3+} + \mathrm{Fe}^{3+} + \mathrm{Ca}^{2+} + \mathrm{Na}^{+}\right]_{\{hk0\}} \quad (3)$$

Furthermore, compositional differences between $\{hk0\}$ and $\{\bar{1}11\}$ sectors are generally larger than those within individual sectors, suggesting that only one family of sectors is likely to have faithfully recorded the conditions of clinopyroxene formation (e.g., Welsch *et al.*, 2016).

Experimental samples

Phase proportions, H_2O contents and fO_2 conditions

Experimental phase proportions were estimated by mass balance, including metallic Fe as a phase in order to evaluate the degree of Fe exchange with capsule materials. Melt fraction decreases steadily as a function of decreasing *T* for all combinations of *P* and capsule type (Table 1), though experiments performed in AuPd capsules have higher melt fractions than those performed in graphite-Pt double capsules at the same *P*–*T* conditions. With the exception of 100-MPa experiments in graphite-Pt double capsules, clinopyroxene was the liquidus phase in all experimental series in which crystals formed; no crystals grew in AuPd-capsule experiments at 100 MPa. Fe exchange between experimental samples and capsule materials was generally minimal: only two experiments in AuPd capsules experienced >10 % relative losses of Fe. No Fe was lost from experiments in graphite-Pt double capsules (Table 1).

Experimental redox conditions were verified using a range of approaches (Table 1). Experiments in graphite-Pt double capsules were theoretically buffered at or below CCO (i.e. at or below ~QFM−1.7; Holloway *et al.*, 1992; Jakobsson and Óskarsson, 1994). H_2O contents of superliquidus glasses (0.04–0.08 wt.% H_2O; Table 1) are consistent with reducing conditions of ~QFM−2.7 and ~QFM−2.1 at 100 and 300 MPa respectively according to the relationship between aH_2O and fO_2 in closed-capsule IHPV (Botcharnikov *et al.*, 2005). Glass $Fe^{3+}/\Sigma Fe$ values in olivine-bearing runs estimated using $K_{D_{ol-liq}}^{Mg-Fe}$ values calculated with the model of Toplis (2005) indicate slightly more oxidising conditions of QFM−0.7 to

QFM−0.9 and QFM−1.0 at 100 and 300 MPa respectively when converted into fO_2 with the model of Kress and Carmichael (1991). However, both aH_2O- and olivine-based methods of fO_2 estimation have uncertainties of at least half a log unit and, in the case of the latter, even small overestimations of $K_{D_{ol-liq}}^{Mg-Fe}$ (e.g., by 0.01) can inflate fO_2 estimates by more than a log unit. It is thus likely that our graphite-Pt-double-capsule experiments were successfully buffered close to CCO.

Based on previous work, we expected superliquidus experiments in AuPd capsules to be buffered close to QFM+1 given that ~0.5 wt.% H_2O is typically produced at high-*P*, high-*T* conditions with this capsule design (Botcharnikov *et al.*, 2005; Husen *et al.*, 2016). Using the approach described above for graphite-Pt-double-capsule experiments, superliquidus glass H_2O contents of 0.50–1.05 wt.% (100 MPa) and 0.64–0.68 wt.% (300 MPa) generated by the reduction of Fe_2O_3 in the starting glass powder indicate that slightly more oxidising experimental fO_2 conditions of QFM+1.5 to QFM+2.7 and QFM+1.3 to QFM+1.4 were achieved in AuPd capsules at 100 and 300 MPa respectively (Table 1). Converting glass $Fe^{3+}/\Sigma Fe$ values determined by colorimetry into fO_2 with the model of Kress and Carmichael (1991) returns similar fO_2 estimates: superliquidus glass $Fe^{3+}/\Sigma Fe$ values of 0.23–0.24 and 0.23–0.25 are indicative of fO_2 conditions of QFM+1.3 to QFM+1.5 and QFM+1.5 to QFM+1.8 at 100 and 300 MPa respectively. Oxygen fugacities were also estimated from capsule compositions (e.g., Grove, 1981), allowing us to evaluate the conditions prevailing during subliquidus experiments. However, redox conditions estimated for superliquidus experiments with the AuPdFe solution model of Barr and Grove (2010) are systematically ~0.6 log units lower than those obtained from colorimetric analyses. Given the coherence between fO_2 conditions estimated from glass H_2O and $Fe^{3+}/\Sigma Fe$ values, we conclude that superliquidus experiments were performed close to QFM+1.5 and that the model of Barr and Grove (2010) underestimates fO_2 at the conditions we investigated, possibly because it was

calibrated on lower-Fe systems than the 2014–2015 Holuhraun lava. Capsule compositions nevertheless suggest that low-*F* experiments may have attained fO_2 conditions about half a log unit higher than those at superliquidus conditions, consistent with the crystallisation of anhydrous phases resulting in higher residual glass H_2O concentrations (e.g., Whitaker *et al.*, 2007). Overall, we estimate that most of our AuPd-capsule experiments equilibrated at ~QFM+1.5 under slightly more oxidising conditions than initially planned.

Glass, olivine and plagioclase compositions

Experimental glass compositions are shown in Fig 5 alongside published matrix glass and melt inclusion compositions (Halldórsson *et al.*, 2018; Hartley *et al.*, 2018). Compositional variability in glass analyses from individual capsules is comparable with estimates of analytical uncertainty, indicating that equilibrium was equally well approached throughout our experimental samples (Supplementary Material). Down-*T* compositional trends defined by experimental glasses depend strongly on *P* and capsule type. In general, low-*P* experiments reproduce natural matrix glass compositions better then high-*P* experiments, with the notable exception that no crystals were produced in AuPd-capsule experiments at 100 MPa. Experiments in graphite-Pt double capsules also replicate natural compositions better than those in AuPd capsules: glasses produced in AuPd capsules at 300 and 600 MPa are enriched in Al_2O_3 with respect to natural compositions whereas those produced in graphite-Pt double capsules at 100 and 300 MPa are not (Figs 5a and 5e). Magmatic liquid compositions (i.e. matrix glasses with >6 wt.% MgO) were approximated best by experiments at ≥1160 °C.

Experimental olivine and plagioclase compositions are shown in Fig. 6 alongside published compositions (Halldórsson *et al.*, 2018). As for experimental glasses, olivine and plagioclase crystals from individual capsules exhibit generally limited compositional variability (Supplementary Material). There are, however, two exceptions. Firstly, some

plagioclase crystals formed at 600 MPa and 1140 °C in AuPd capsules are compositionally variable, possibly as a result of disequilibrium crystallisation. Secondly, some plagioclase analyses return variably elevated FeO* contents as a result of secondary fluorescence from surrounding Fe-rich glasses – polished plagioclase crystals are often thinner than the excitation volume of typical EPMA spots (i.e. <2 μm).

Olivine was only produced during lower-*T* runs in graphite-Pt double capsules (Fig. 4a); no olivine formed in AuPd-capsule experiments. Although natural macrocryst cores are within the range of compositions predicted to be in equilibrium with the starting glass powder at experimental *P*–fO_2 conditions according to the $K_D^{Mg–Fe}_{ol–liq}$ model of Toplis (2005) (X_{Fo} = 0.74–0.79), experimentally produced olivines are typically more evolved and have X_{Fo} contents comparable with natural macrocryst rims (X_{Fo} ~ 0.64–0.72). Olivines produced at 100 MPa are more similar to natural olivine cores than those produced at 300 MPa (Fig. 6a).

Although plagioclase crystals were produced under diverse experimental conditions (Fig. 6b), they exhibit only modest compositional variability (X_{An} = 0.61–0.69). Plagioclase stability nonetheless depends strongly on *P* in AuPd-capsule experiments, with plagioclase joining the crystallising assemblage at >1180 °C, >1140 °C and <1140 °C at 600, 300 and 100 MPa respectively. This probably reflects the effect of small amounts of H_2O on plagioclase stability (Table 1; Almeev *et al.*, 2012). No comparable *P* dependence was observed in graphite-Pt-double-capsule experiments: plagioclase was stable at >1160 °C at both 100 and 300 MPa, reflecting the uniformly low H_2O content of these runs (Supplementary Material; Almeev *et al.*, 2012). According to the model of Namur *et al.* (2012), the starting glass powder would be in equilibrium with plagioclase compositions similar to those observed in microcrysts or evolved macrocryst cores from natural samples (X_{An} ~ 0.75; Fig. 6b; Halldórsson *et al.*, 2018). However, most experimental plagioclase crystals are more evolved than predicted compositions and are instead comparable with

natural macrocryst rims (Fig 6b). Plagioclase crystals produced at 1160 °C and 100 MPa in graphite-Pt double capsules most closely approach microcryst and evolved macrocryst core compositions (X_{An} ~ 0.68; Fig. 5b; Halldórsson *et al.*, 2018).

Clinopyroxene compositions

With the exception of experiments performed at 100 MPa in graphite-Pt double capsules, clinopyroxene was the liquidus phase for all combinations of P and fO_2 under which crystals formed (Figs. 4b, 4c, 7 and 8). Mean clinopyroxene compositions span the $Mg\#_{cpx}$ range 0.69–0.80. The highest-Mg experimental clinopyroxenes have $Mg\#_{cpx}$ contents comparable to those in natural macrocryst cores ($Mg\#_{cpx}$ ~ 0.80; Halldórsson *et al.*, 2018). In contrast, the lowest-Mg clinopyroxenes have similar compositions to macrocryst rims ($Mg\#_{cpx}$ ~ 70). However, simple comparisons between natural and experimental clinopyroxenes are otherwise impeded by the complex dependencies of clinopyroxene compositions on P, T and fO_2. For example, mean clinopyroxene Na contents depend on P (e.g., Blundy *et al.*, 1995; Putirka *et al.*, 1996), with crystals produced at 100 and 600 MPa containing respectively less and more Na than natural crystals (Fig. 8f); natural Na contents are best approximated by the products of 300-MPa experiments at 1180 °C. In contrast, mean clinopyroxene Ca and Fe contents appear to be more sensitive to T (or F) than P: crystals formed during our lowest-F runs, i.e. those from low-T runs in graphite-Pt double capsules at 300 MPa and AuPd capsules at 600 MPa, have lower Ca but higher Fe contents than natural macrocryst cores (Figs. 8d and 8e). Finally, clinopyroxenes from graphite-Pt-double-capsule experiments are consistently richer in Ti but poorer in Al than those from AuPd-capsule experiments performed under similar conditions (Figs. 8a and 8b). Overall, mean experimental clinopyroxene compositions lie closer to natural clinopyroxene analyses from $\{hk0\}$ prism sectors than $\{\bar{1}11\}$ hourglass sectors. However, mean compositions provide only partial descriptions of the true chemical complexity present in experimental clinopyroxenes.

Although phase equilibria studies on tholeiitic systems have generally reported mineral compositions as mean values of multiple spot analyses, it has been noted for some decades that clinopyroxene compositions are typically more heterogeneous than can be explained by analytical uncertainty alone (e.g., Grove and Bryan, 1983; Grove *et al.*, 1992; Villiger *et al.*, 2004; Berndt *et al.*, 2005; Ulmer *et al.*, 2018). We therefore report all the spot analyses we made on clinopyroxenes (n = 16–46 per sample) in order to document the full compositional diversity present in our experimental samples (Fig. 10 and Supplementary Material). For example, clinopyroxene Al and Ca contents are much more variable than corresponding analytical uncertainties regardless of experimental conditions (Figs. 10 a–f). In the case of the 300-MPa experiment carried out in a graphite-Pt double capsule at 1180 °C, the range of experimental clinopyroxene compositions is broadly comparable with that observed in natural samples (Figs. 10c, 10f and 10i). Clinopyroxenes from the lowest-F experiment performed in a graphite-Pt double capsule at 300 MPa and 1140 °C show the greatest compositional variability (expressed as a mean-normalised standard deviation) in geobarometry-critical Na contents (Fig. 11a). Moreover, clinopyroxenes from graphite-Pt-double-capsule experiments have consistently more variable Al_2O_3 contents than those produced in AuPd-capsule experiments (Fig. 11b).

Mean clinopyroxene Fe^{3+} contents and $Fe^{3+}/\Sigma Fe$ values estimated using the approach of Lindsley (1983) are shown in Fig. 12. Although $Fe^{3+}/\Sigma Fe$ values estimated by stoichiometry can be subject to absolute uncertainties of up to 25% (e.g., McGuire *et al.*, 1989), it was still possible for us to resolve compositional differences between clinopyroxenes produced under different P–fO_2 conditions. Clinopyroxenes from experiments performed under reducing conditions in graphite-Pt double capsules contain no consistently resolvable Fe^{3+}, resulting in estimated $Fe^{3+}/\Sigma Fe$ values of 0.00±0.04(1σ). In contrast, clinopyroxenes from AuPd-capsule experiments performed under moderately oxidising

conditions contain appreciable amounts of Fe^{3+}: clinopyroxenes produced at 300 MPa return estimated $Fe^{3+}/\Sigma Fe$ values of 0.18±0.01(1σ) whereas those produced at 600 MPa return slightly lower $Fe^{3+}/\Sigma Fe$ values of 0.10±0.02(1σ). For comparison, we estimate that natural clinopyroxenes from sample MSR161014 have $Fe^{3+}/\Sigma Fe$ values of approximately 0.05–0.25 using the same approach (Fig. 12b).

DISCUSSION

Clinopyroxene in phase equilibria experiments

Compositional variability and sector zoning

Experimental clinopyroxenes produced in this study are often too small for zoning to be resolved clearly, even by FEG-SEM (Fig. 4). Nevertheless, many experimental clinopyroxenes show heterogeneous BSE intensities. Although some crystals show hints of concentric zoning potentially formed during thermal cycling (Figs. 4a and 4c), patchy zoning is more pervasive (Figs. 4a and 4d), suggesting that sector zoning is mainly responsible for the chemical systematics we observe rather than concentric zoning (e.g., Ulmer *et al.*, 2018). Moreover, the compositional variability within clinopyroxenes from individual experiments is more consistent with sector zoning than concentric zoning (Nakamura, 1973; Ubide *et al.*, 2019): compositional arrays lie between two end-members that are Mg-poor but Al-rich (i.e. rich in non-quadrilateral components) on one hand and Mg-rich but Al-poor (i.e. rich in quadrilateral components) on the other (Fig. 10). Clinopyroxene compositions from some high-*F* experiments (e.g., 300 MPa and 1180 °C in a graphite-Pt double capsule) also occupy a similar region of geochemical space to natural crystals with well-developed sector zoning (Figs. 8 and 10). Unfortunately, the exact nature of clinopyroxene variability in our experimental samples remains unclear. Do the compositional arrays observed reflect complex internal zoning, or do they represent variably mixed analyses of otherwise compositionally

distinct zones? It is nevertheless certain that large numbers of spot analyses (>20 and ideally >40) are required to meaningfully characterise experimental clinopyroxenes.

Disequilibrium in nominally equilibrium experiments

Dynamic crystallisation experiments (i.e. those performed under variable T conditions) demonstrate that clinopyroxene compositions depend strongly on the degree of undercooling they experience during crystallisation as well as on absolute P–T–X conditions (Grove and Bence, 1977; Lofgren *et al.*, 2006; Mollo *et al.*, 2018). Specifically, EnFs, CaTs and Jd component contents in augitic clinopyroxenes increase at the expense of DiHd component contents with increasing undercooling (Mollo *et al.*, 2010). This deviation of mean clinopyroxene compositions away from equilibrium values has important implications for geothermobarometry: calculations performed on crystals grown at high degrees of undercooling overestimate true P–T conditions because of the incorporation of excess Jd component (Mollo *et al.*, 2010, 2013). Although Mollo *et al.* (2010) did not report compositional zoning in the products of their dynamic crystallisation experiments, others have described strong correlations between the degree of nominal undercooling (i.e. the difference between the liquidus T and the experimental T, ΔT) and the intensity of compositional zoning in isothermal crystallisation experiments. For example, Kouchi *et al.* (1983) observed that $\{\bar{1}11\}$ sectors in Al-rich clinopyroxenes grown at 13 °C < $\Delta T \leq$ 25 °C are depleted in Al with respect to $\{hk0\}$ sectors. At $\Delta T >$ 25 °C they observed that the sense of compositional zoning reversed, highlighting clinopyroxene's sensitivity to undercooling. Moreover, their observations indicate that the incorporation of EnFs, CaTs and Jd components during disequilibrium growth of clinopyroxene may partially reflect an intensification of sector zoning rather than a simple shift in bulk composition.

Our experiments were designed to reproduce equilibrium crystallisation conditions. That is, after using low amplitude (±10 °C) thermal cycling to promote the growth of large

crystals (Erdmann and Koepke, 2016), experiments were held at their final target *T* until quenching. However, both the texture and compositional variability of experimental clinopyroxenes depend on *T* and *F*, implying that they reflect the deviation of *T* below the clinopyroxene liquidus *T* (i.e. the degree of undercooling *sensu lato*) experienced at the onset of crystallisation. For example, small numbers of large clinopyroxene crystals were produced in high-*T*, high-*F* experiments (Fig. 4c), whereas numerous small crystals were produced in low-*T*, low-*F* experiments (Fig. 4d), a relationship consistent with changes in the relative influences of nucleation and growth with increasing undercooling (Kirkpatrick, 1976; Cashman, 1993; Hammer, 2008; Mollo and Hammer, 2017). That is, nucleation appears to have dominated over growth in experiments performed well below the clinopyroxene liquidus (low-*F*) when thermodynamic barriers to nucleation could be readily overcome, though competition for chemical nutrients may have also contributed towards restricting crystal sizes (Mollo and Hammer, 2017). In contrast, when experiments were performed close to the clinopyroxene liquidus (high-*F*), growth dominated over nucleation. Importantly, the same magnitude of thermal cycling was applied to all samples, meaning that even if cycling affected the details of crystal nucleation and growth in individual experiments, it is unlikely to account for systematic differences in clinopyroxene properties as a function of *T* or *F*. Indeed, other studies reporting compositional heterogeneity in experimental clinopyroxenes from tholeiitic systems did not apply thermal cycling (e.g., Grove *et al.*, 1992; Berndt *et al.*, 2005).

The compositional variability in clinopyroxenes produced in our lowest-*F* experiment performed in a graphite-Pt double capsule at 300 MPa and 1140 °C ($F \sim 0.5$) highlights that clinopyroxenes from so-called equilibrium experiments can sometime preserve strongly disequilibrium compositions (Fig. 11). However, highly variable compositions are restricted to nominally dry experiments in graphite-Pt double capsules. Given that H_2O acts to reduce

chemical disequilibrium around growing crystals by increasing elemental diffusivities, decreasing melt viscosities and reducing the degree of undercooling by depressing liquidi (Hammer, 2008), we suggest that the presence of small amounts of H_2O can explain the differences in clinopyroxene compositional variability we observe. For example, the presence of 1 wt.% H_2O may increase Si and Mg diffusivities in silicate melts by factors of approximately three and five respectively (Zhang *et al.*, 2010). We thus propose that the 0.5–1.0 wt.% H_2O present in the melts of our AuPd-capsule experiments was sufficient to prevent the crystallisation of disequilibrium clinopyroxene compositions like those observed in the products of nominally anhydrous graphite-Pt-double-capsule experiments (~0.1 wt.% H_2O; Fig. 11) by allowing chemical nutrients to be delivered to growing crystal faces at sufficiently fast rates to maintain near-equilibrium conditions.

Oxygen fugacity and clinopyroxene $Fe^{3+}/\Sigma Fe$ values

Experiments in graphite-Pt double capsules at 300 MPa are thought to have attained fO_2 conditions close to the CCO buffer – $Fe^{3+}/\Sigma Fe \sim 0.08$ according to calculations following Kress and Carmichael (1991) – within a few hours (e.g., Médard *et al.*, 2008). Equivalent calculations for 300-MPa AuPd-capsule experiments buffered at approximately QFM+1.5 predict melt $Fe^{3+}/\Sigma Fe$ values of ~0.25 that are consistent with colorimetric analyses of superliquidus experiments (Table 1). This difference in melt $Fe^{3+}/\Sigma Fe$ values is also reflected in clinopyroxene $Fe^{3+}/\Sigma Fe$ values estimated by stoichiometry (Lindsley, 1983), which are 0.00±0.04(1σ) for 300-MPa experiments in graphite-Pt double capsules and 0.18±0.01(1σ) for 300-MPa experiments in AuPd capsules (Figs. 12a and 12b). Ferric iron is thus an important constituent of clinopyroxenes formed at P–T–fO_2 conditions relevant to the evolution of natural tholeiites; simply assuming that all Fe in clinopyroxenes occurs as Fe^{2+} is invalid for tholeiitic systems, a situation likely to be even worse for oxidised alkalic and calc-alkaline systems (e.g., Kelley and Cottrell, 2012; Longpré *et al.*, 2017).

High-Fe^{3+} clinopyroxenes produced in AuPd capsules are richer in Al and Ca than low-Fe^{3+} clinopyroxenes produced in graphite-Pt double capsules under the same *P–T* conditions (Figs. 12c and 12d). Although plagioclase co-crystallisation affects clinopyroxene compositions to some degree, comparing clinopyroxene-bearing experiments performed at 300 MPa and similar *F* conditions to mitigate the effects of other phases reveals similar overall trends. In contrast, there is no clear relationship between redox conditions and clinopyroxene Na contents in our experimental data (Fig. 12e). Within the range of investigated fO_2 conditions (approximately CCO to QFM+1.5), our results thus suggest that Fe^{3+} is incorporated into augitic clinopyroxene alongside Ca and Al as Ca-Fe-Tschermak's component (CaFeTs; $CaFe^{3+}AlSiO_6$; Luth and Canil, 1993; Blundy *et al.*, 1995; Mollo *et al.*, 2018). We find no evidence for the significant incorporation of Fe^{3+} as Na-bearing Ae component. Therefore, assuming that all Na in clinopyroxene is present as Jd component appears to be valid in tholeiitic magmas as oxidised as QFM+1.5. Whether this assumption still holds in oxidised alkalic systems like the Canary Islands where clinopyroxene $Fe^{3+}/\Sigma Fe$ values can exceed 0.5 (Weis *et al.*, 2015) remains to be addressed.

Geothermobarometry and clinopyroxene–liquid equilibria

If geothermobarometric models are well calibrated, then they should be able to reproduce imposed *P–T* conditions when applied to experimental products. By applying various models to the products of experiments performed at crustal *P* conditions (100–800 MPa), Neave and Putirka (2017) observed that previously published Jd-in-clinopyroxene geobarometers consistently overestimated experimental *P* conditions for runs performed at ≤700 MPa. This led them to propose a new geobarometer optimised for mafic and alkali-poor magmas stored at crustal depths. However, they only tested their model using mean compositions of experimentally produced clinopyroxenes that, as demonstrated above, only offer partial descriptions of clinopyroxene compositions. In order to provide a more complete test of the

geothermobarometric approach recommended by Neave and Putirka (2017) – iteratively solving their equation 1 with equation 33 from Putirka (2008) – we applied it to all clinopyroxene–liquid pairs measured in our experimental products (Fig. 13).

For any given set of *P*–*T*–fO_2 conditions, geothermobarometric calculations on individual clinopyroxene–liquid pairs return positively correlated and broadly distributed *P*–*T* arrays, reflecting the interdependence of geobarometric and geothermometric models. In some cases, such as for experiments performed in AuPd capsules at 300 MPa (Fig. 13a), *P*–*T* estimates are dispersed to an extent commensurate with the prediction errors of geothermobarometric models: calibrations of equation 1 from Neave and Putirka (2017) and equation 33 from Putirka (2008) are associated with standard errors of estimate (SEEs) of ±140 MPa and ±27 °C respectively. In other cases, *P*–*T* estimates vary well beyond model SEEs. For example, low-*T* experiments in graphite-Pt double capsules are associated with large ranges of estimated *P*–*T* conditions (Figs. 13c and 13d). In the most extreme case, clinopyroxene analyses from the 300-MPa experiment at 1140 °C return bimodal *P* and *T* distributions with absolute ranges greater than 100–900 MPa and 1140–1210 °C respectively (Fig. 13d). The deviation of calculated *P*–*T* conditions from imposed conditions correlates with the degree of geochemical variability within clinopyroxene populations. Given that clinopyroxene variability is linked to both the melt H_2O content and the deviation below the clinopyroxene liquidus *T*, spreads in estimated *P*–*T* values are thus linked to the degree of disequilibrium experienced during crystallisation (e.g., Kouchi *et al.*, 1983; Mollo *et al.*, 2010). Despite this, mean estimated *P*–*T* conditions are almost always within 1SEE of experimental values; all mean *P*–*T* conditions are well within 2SEE. Therefore, experiments performed at 100, 300 and 600 MPa can be readily distinguished from each other based on the results of geobarometric calculations. Pressure conditions estimated from AuPd-capsule experiments also show no systematic *P* differences with respect to those performed in

graphite-Pt double capsules, lending further credence to our suggestion that Fe^{3+} is incorporated as CaFeTs component rather than Ae component under the conditions studied.

The wide ranges of *P*–*T* values estimated from clinopyroxene compositions obtained at fixed experimental conditions reinforce previous suggestions that using only $K_{D_{cpx-liq}}^{Mg-Fe}$ values to check for clinopyroxene–liquid equilibrium in natural rocks is inadequate (Mollo *et al.*, 2010, 2013; Winpenny and Maclennan, 2011; Neave and Putirka, 2017). However, that >65% of clinopyroxene analyses return *P* values within 1SEE of the imposed conditions does indicate that experimental conditions were recorded faithfully in some cases; the low-*F*, 300-MPa experiment performed in graphite-Pt double capsules at 1140 °C represents a possible exception to this. The departure of individual clinopyroxene analyses from equilibrium was evaluated using equations 6 and 7 from Mollo *et al.* (2013) that describe DiHd and EnFs component equilibria and equation 3.4 from Putirka (1999) that describes CaTs component equilibrium. We note that these descriptions of clinopyroxene–liquid equilibria have been calibrated on mean experimental clinopyroxene compositions and without considering the effects of Fe^{3+}. However, they represent the most complete empirical descriptions of clinopyroxene–liquid equilibria currently available and have been validated using experiments performed at low degrees of undercooling that are unlikely to have experienced appreciable disequilibrium crystallisation (Mollo *et al.*, 2013).

Tests for DiHd component equilibrium are shown in Fig. 14; equivalent plots for EnFs and CaTs components are provided in the Supplementary Material. Clinopyroxene analyses from most experiments performed in AuPd capsules are close to being in DiHd component equilibrium (Figs. 14a and 14b), though some analyses from 600-MPa experiments have DiHd component contents slightly more than 1SEE above predicted values. In contrast, almost all clinopyroxene analyses from graphite-Pt-double-capsule experiments contain DiHd component contents more than 1SEE below predicted values (Figs. 14c and

14d). Such deviations are frequently greater than 2SEE in the cases of clinopyroxenes formed at 1140 and 1160 °C. The only experiment in graphite-Pt double capsules to return a meaningful number of clinopyroxene analyses in DiHd component equilibrium with their surrounding melt was performed under high-*F* conditions at 1180 °C and 300 MPa.

Internally consistent clinopyroxene geothermobarometry

With the aim of developing an internally consistent approach for performing clinopyroxene–liquid geothermobarometry on natural tholeiites, we tested the effect of filtering the results of our geothermobarometric calculations on experimentally produced clinopyroxene–liquid pairs for multicomponent equilibrium (e.g., Hildner *et al.*, 2012; Neave *et al.*, 2013; Neave and Putirka, 2017; Halldórsson *et al.*, 2018; Shane and Coote, 2018). Glass and clinopyroxene compositions were considered to be in equilibrium if observed DiHd, EnFs and CaTs component values were within 1SEE of predicted values (i.e. within ±0.06, ±0.05 and ±0.03 for DiHd, EnFs and CaTs components respectively; Putirka, 1999; Mollo *et al.*, 2013). Thresholds for equilibrium were set at 1SEE for two reasons. Firstly, filters based on calibration statistics account for model uncertainties explicitly, whereas filters based on arbitrary thresholds do not. Indeed, some previous studies have over-filtered for CaTs component equilibrium when using arbitrary filters (e.g., Neave and Putirka, 2017). Secondly, adopting a conservative approach (i.e. setting thresholds at 1SEE instead of 2SEE) reduces the risk of returning false positives.

The results of filtering experimental clinopyroxene–liquid pairs are shown alongside unfiltered data in Fig. 13. Two key trends can be identified: firstly, high-*F*, high-*T* experiments are more likely to pass equilibrium filters than low-*F*, low-*T* experiments; and secondly, experiments in AuPd capsules return a greater number of reliable *P*–*T* estimates than experiments in graphite-Pt double capsules. The likelihood of clinopyroxene–liquid pairs passing equilibrium tests thus correlates inversely with melt H_2O content and the

deviation from clinopyroxene liquidus *T*, two properties related to the ability of crystals to crystallise under near-equilibrium conditions (see above; Hammer, 2008). That is, the greatest number of equilibrium pairs are found in experimental products synthesised close to the clinopyroxene liquidus in the presence of ≥0.5 wt.% H_2O. Encouragingly, mean *P* conditions recorded by clinopyroxene–liquid pairs passing multicomponent equilibrium tests all lie within 1SEE of imposed experimental conditions. Filtered *P* estimates are much less dispersed than unfiltered *P* estimates and mean *T* conditions are mostly within 1SEE of experimental values, especially for higher-*T* experiments. Our findings nonetheless suggest that clinopyroxene geothermometer calibrations could be improved by re-evaluating relationships between *T* and *X* in Fe^{3+}-bearing systems; obtaining precise estimates of clinopyroxene $Fe^{3+}/\Sigma Fe$ values will be vital if clinopyroxene geothermobarometry is to be developed further.

Filtering for multicomponent equilibrium thus provides an efficient way of eliminating disequilibrium clinopyroxene compositions from geothermobarometric calculations on tholeiitic as well as alkalic samples (cf. Mollo *et al.*, 2013). Importantly, no *a priori* filtering of clinopyroxene data is required to obtain coherent *P–T* estimates. In other words, there is no need to assume that one family of sector zones records equilibrium crystallisation while another does not (e.g., Neave *et al.*, 2015). When performing calculations on natural clinopyroxene–liquid pairs, we therefore recommend checking for equilibrium in DiHd, EnFs and CaTs components as well as ensuring that $K_{D_{cpx-liq}}^{Mg-Fe}$ values are within a sensible range [e.g., within 0.03 of values from equation 35 of Putirka (2008)]. We include a spreadsheet in the Supplementary Material to facilitate such calculations.

Implications for the 2014–2015 Holuhraun eruption

Geothermobarometry

Clinopyroxene–liquid geothermobarometry was performed on natural clinopyroxenes from MSR161014 using an iterative melt-matching algorithm that refines storage conditions over multiple cycles of equilibrium testing and geothermobarometry that is described in detail by Neave *et al.* (2013) and Neave and Putirka (2017). Clinopyroxene compositions were tested for equilibrium against the matrix glass dataset reported by Halldórsson *et al.* (2018) and were considered to be in equilibrium if: 1) $K_{D_{cpx-liq}}^{Mg-Fe}$ values were within 0.03 of equilibrium values calculated assuming a melt $Fe^{3+}/\Sigma Fe$ value of 0.15 (Putirka, 2008; Bali *et al.*, 2018); and 2) DiHd-, EnFs- and CaTs-component contents were within 1SEE of predicted values (Putirka, 1999; Mollo *et al.*, 2013). The R code used to perform these calculations is available from the authors on request. We also performed geothermobarometric calculations with the spreadsheet provided in the Supplementary Material in order to test if a simpler approach would yield comparable results to those from the more rigorous melt-matching algorithm. In this case, we paired clinopyroxene compositions with the mean matrix glass composition reported by Halldórsson *et al.* (2018).

The results of geothermobarometric calculations are summarised in Fig. 15. In the case of calculations with the melt-matching algorithm (Fig. 15a), we report *P–T* estimates for each clinopyroxene analysis to which equilibrium liquids could be matched (4–274 matches per clinopyroxene; median = 59). When multiple matches were found for individual analyses, we report mean *P–T* estimates. In the case of spreadsheet calculations (Fig. 15b), we report *P–T* estimates for clinopyroxene analyses that passed equilibrium tests and distinguish results from clinopyroxene rims (but not outermost rims) that are likely to have been in textural equilibrium with carrier liquids (i.e. matrix glass) during their crystallisation (e.g., Klügel *et al.*, 2005). Individual *P–T* estimates calculated with both methods form tight arrays, confirming that matched clinopyroxenes do indeed represent a single macrocryst population. The reduced scatter in Fig. 15a with respect to that in Fig. 15b results from the use of iterative

calculations and is not of geological significance, however. Mean *P–T* estimates lie in the centre of calculated ranges for both approaches and are almost identical to previous estimates (Halldórsson *et al.*, 2018): 232 MPa and 1161 °C for calculations with the melt-matching algorithm and 208 MPa and 1161 °C for spreadsheet calculations (Fig. 15). *P–T* estimates are distributed in proportion with the prediction errors of the geothermobarometric models used (±140 MPa and ±27 °C), albeit with a slight skew towards lower *P–T* conditions for calculations with the melt-matching algorithm. The only significant difference between the approaches is that the spreadsheet calculations failed to exclude two compositions that returned spurious, negative pressures. Mean *P–T* estimates from rims in textural equilibrium with their carrier melts are indistinguishable from those calculated using the full dataset. However, in agreement with previous observations (Halldórsson *et al.*, 2018), we note that *P–T* conditions obtained from these could be less dispersed than those obtained from the dataset as a whole. Combining textural constraints with tests for multicomponent chemical equilibrium is thus likely to return the most precise *P–T* estimates from volcanic samples.

Clinopyroxene macrocrysts analysed in this study appear to have formed within a narrow *P* interval centred at ~230 MPa based on calculations using our melt-matching algorithm. That is, the dispersion in estimated *P–T* values reflects a combination of analytical uncertainties, geothermobarometric uncertainties and disequilibrium crystallisation; we see no evidence for polybaric crystallisation in clinopyroxene macrocrysts from MSR161014. Importantly, the 2014–2015 Holuhraun lava's extreme compositional homogeneity (Halldórsson *et al.*, 2018) suggests that our findings can be justifiably extrapolated to the eruption as a whole. Our refined storage pressure estimates are wholly consistent with independent petrological estimates based on modelling OPAM thermal minima (210±70(1σ) MPa; Hartley *et al.*, 2018). Moreover, assuming a mean oceanic crustal density of 2860 kg m^{-3} (Carlson and Herrick, 1990), our preferred storage *P* estimate of 230±140(1SEE) MPa

corresponds to depth of 8.3±5.0 km, which overlaps with geodetic and seismic signals of magma storage and movement in the Bárðarbunga volcanic system (8–12 km; Ágústsdóttir *et al.*, 2016; Guðmundsson *et al.*, 2016; Sigmundsson *et al.*, 2015).

Geothermobarometric results from the melt-matching algorithm are compared with results from spreadsheet calculations performed without applying equilibrium tests in Fig. 16. Most clinopyroxene analyses for which equilibrium liquids could be found are from $\{hk0\}$ prism sectors (Figs. 3 and 16). When equilibrium liquids could be found for analyses from $\{\overline{1}11\}$ hourglass sectors, the compositional divergence from analyses in $\{hk0\}$ prism sectors was minimal. Inspecting unfiltered geothermobarometric results from spreadsheet calculations highlights the effect of disequilibrium crystallisation on *P* estimates: low DiHd component contents in $\{\overline{1}11\}$ sectors are associated with low Jd component contents, shifting clinopyroxene–liquid Jd component exchange coefficients away from equilibrium, resulting in the calculation of geologically implausible negative pressures. Thus, disequilibrium crystallisation has the opposite effect on *P* estimates from clinopyroxene macrocrysts from the 2014–2015 Holuhraun lava when compared with that predicted from dynamic crystallisation studies (Baker and Grove, 1985; Mollo *et al.*, 2010, 2013). Namely, geobarometric calculations on disequilibrium compositions from our samples are likely to underestimate rather than overestimate true storage pressures. This is because disequilibrium manifests primarily in sector zone development rather than the bulk modification of clinopyroxene compositions typically reported in previous work.

Magma assembly

Clinopyroxene sector zoning theoretically records information about the degree of undercooling experienced during crystallisation (e.g., Welsch *et al.*, 2016). However, too few experimental data are currently available to robustly invert clinopyroxene sector zoning patterns for cooling histories in all but the simplest systems (Kouchi *et al.*, 1983).

Nevertheless, comparing the findings of Kouchi *et al.* (1983) with the compositional systematics observed in our natural clinopyroxenes suggests that crystallisation probably occurred at low degrees of undercooling (perhaps on the order of 25 °C or less). It is this probable that crystallisation was driven purely by cooling with no contribution from H_2O exsolution (cf. Applegarth *et al.*, 2013), which is consistent with the magma's modest pre-eruptive H_2O content (<0.6 wt.%; Bali *et al.*, 2018): H_2O would have only exsolved during final ascent (<40 MPa; Hartley *et al.*, 2018), too late to affect the crystallisation of clinopyroxene macrocrysts considered here.

Compositional heterogeneity in clinopyroxene macrocrysts is not restricted to the development of sector zoning: concentric zoning within $\{hk0\}$ sectors is characterised by variability in Ti, Al, Cr and Fe contents at relatively constant Mg contents (Figs. 7, 8 and 16). Specifically, some concentric zones are enriched in non-quadrilateral components, consistent with disequilibrium crystallisation described by the following kinetically controlled exchange (e.g., Mollo *et al.*, 2013):

$$[\mathrm{Di} + \mathrm{Hd}]_{\mathrm{cpx}} + \mathrm{melt} \rightleftharpoons [\mathrm{Jd} + \mathrm{CaTs} + \mathrm{CaFeTs} + \mathrm{CaTiTs} + \mathrm{En}]_{\mathrm{cpx}} \quad (4)$$

Given that concentric zoning can be traced through both $\{hk0\}$ and $\{\bar{1}11\}$ sectors (Fig. 3), we suggest that clinopyroxene crystallisation took place at low but nonetheless variable degrees of undercooling, leading not only to the development of $\{\bar{1}11\}$ sectors with disequilibrium compositions but also to the growth of some concentric zones with disequilibrium compositions, even within $\{hk0\}$ sectors. There are numerous ways that variations in undercooling could have arisen. For example, punctuated recharge of a clinopyroxene-saturated reservoir could have driven cyclical changes in undercooling (Petrone *et al.*, 2016; Ubide and Kamber, 2018). Alternatively, convective stirring within a melt-rich storage region – consistent with the extreme homogeneity of erupted liquids (Halldórsson *et al.*, 2018) – could have transported clinopyroxene macrocrysts through a range of thermally distinct

environments (Couch *et al.*, 2001; Ginibre *et al.*, 2002). Indeed, the euhedral form of many clinopyroxene crystals suggests that they grew in a melt-rich environment rather than within a static crystal mush (e.g., Holness *et al.*, 2019). Therefore, although compositional variability within clinopyroxene macrocrysts complicates geothermobarometric calculations, it does encode information about magma reservoir dynamics.

Clinopyroxene textures, compositions and geothermobarometry suggest that the magma was stored at ~1160 °C prior to eruption – conditions under which olivine, plagioclase and clinopyroxene crystallised simultaneously at the basaltic thermal minimum. The sense of sector zoning suggests that the degree of undercooling was low (perhaps 25 °C or less) and that the magma could not have cooled from temperatures much above the clinopyroxene liquidus (~1180 °C at ~230 MPa according to our experiments) upon arrival in the shallow crust. Clinopyroxene macrocrysts nevertheless record fluctuations in storage conditions, resulting in the development of complex concentric zoning that is mirrored in the oscillatory zoning of cogenetic plagioclase macrocryst rims (Halldórsson *et al.*, 2018). However, our geothermobarometric results and an absence of progressive core-to-rim zoning (with the exception of outermost rims formed during lava emplacement) imply that pre-eruptive storage conditions did not diverge consistently from 230±140(1SEE) MPa and 1161±27(1SEE) °C during the final stages of storage in the magma reservoir. However, not all macrocrysts carried by the 2014–2015 Holuhraun lava formed at these conditions; primitive macrocryst record earlier phases of evolution in different magmatic environments.

Primitive macrocrysts of high-X_{Fo} olivine, high-X_{An} plagioclase and rare high-Mg#$_{cpx}$ clinopyroxene record crystallisation at higher temperatures than the macrocryst assemblage formed immediately prior to eruption (Figs. 5, 6 and 7; Halldórsson *et al.*, 2018). However, the relationship between evolved and primitive macrocrysts is not straightforward. Melt inclusions hosted in primitive macrocrysts record the entrapment of compositionally diverse

melts that cannot be related to erupted liquids and evolved macrocrysts by differentiation along a simple single liquid line of descent (Hartley *et al.*, 2018). Instead, primitive macrocrysts are likely to have been entrained by melts parental to the erupted magma during their ascent through crystal mushes beneath the Bárðarbunga volcanic system (Halldórsson *et al.*, 2018; Hartley *et al.*, 2018), as has been suggested for other Icelandic systems (Hansen and Grönvold, 2000; Halldórsson *et al.*, 2008; Passmore *et al.*, 2012; Neave *et al.*, 2013, 2014). Moreover, observations on Icelandic lavas suggest that evolved and primitive assemblages are typically juxtaposed within weeks of eruption (Hartley *et al.*, 2015, 2016, 2018; Pankhurst *et al.*, 2018), placing a maximum limit on the time taken to crystallise evolved macrocrysts.

Integrating our new observations with published work enables us to propose the following simplified model for the assembly of the 2014–2015 Holuhraun magma. Firstly, melts directly parental to the erupted liquid segregated efficiently from crustal mushes at pressures in excess of 230 MPa. These melts entrained primitive and geochemically diverse macrocrysts during ascent towards their final storage in a reservoir at ~230 MPa (Hartley *et al.*, 2018). Importantly, it appears that no primitive macrocrysts are unambiguously cogenetic with the erupted melt, meaning that the origins if this melt remain frustratingly obscure (Halldórsson *et al.*, 2018). Mixing during ascent may have facilitated the homogenisation of parental melts that subsequently cooled from temperatures close to the clinopyroxene liquidus (~1180 °C) to ~1160 °C, resulting in the crystallisation of olivine, plagioclase and sector-zoned clinopyroxene at low but variable degrees of undercooling. This crystallisation produced the erupted liquid which ultimately carried two discrete macrocryst assemblages to the surface, an equilibrium assemblage formed at ~230 MPa and ~1160 °C and an entrained assemblage formed at higher pressures and temperatures.

CONCLUSIONS

Natural clinopyroxene macrocrysts from the tholeiitic 2014–2015 Holuhraun lava are characterised by both sector and concentric zoning. In contrast with recent work on alkalic systems (e.g., Welsch *et al.*, 2016; Ubide *et al.*, 2019), we observe that sector zoning is characterised by differences in Ca and Na as well as in Ti and Al, with $\{\bar{1}11\}$ hourglass sectors being enriched in EnFs component with respect to $\{hk0\}$ prism sectors. We therefore caution against extrapolating findings from well-studied but not universally representative alkalic systems to geologically more widespread tholeiitic systems.

By quantifying the degree of compositional variability in clinopyroxene crystals produced in experiments on the 2014–2015 Holuhraun lava, we demonstrate that crystals from nominally equilibrium experiments can preserve strongly disequilibrium compositions. The magnitude of clinopyroxene compositional variability in any given experiment depends on both the melt H_2O content and the degree to which the experimental *T* deviates from the clinopyroxene liquidus *T*, indicating that clinopyroxene compositions are controlled by kinetic processes within the melt as well as around crystal–melt interfaces. In future, separating the effects of H_2O and major element composition will help to reconcile seemingly divergent observations on clinopyroxene crystallisation kinetics in different magma types and make sector zoning an effective probe of crystallisation conditions.

Although clinopyroxene $Fe^{3+}/\Sigma Fe$ values estimated by stoichiometry are subject to considerable uncertainties, estimated values up to ~0.2 in our natural and experimental samples demonstrate that Fe^{3+} is a major constituent of augitic clinopyroxenes at naturally relevant fO_2 conditions. The compositional systematics of our experimental clinopyroxenes suggest that Fe^{3+} is incorporated as Ca- and Al-bearing CaFeTs component with minimal incorporation as Na-bearing Ae component. Therefore, assuming that all Na in clinopyroxene occurs as Jd component is justified in tholeiitic systems when fO_2 is below QFM+1.5.

Elevated fO_2 conditions are thus less likely to compromise Jd-in-clinopyroxene geothermobarometry than previously envisaged (Neave and Putirka, 2017).

By combining geothermobarometric models with empirical descriptions of clinopyroxene–liquid equilibria we present an internally consistent and experimentally verified method for performing Jd-in-clinopyroxene geothermobarometry. Our approach avoids having to select equilibrium zones *a priori* by performing geothermobarometry and filtering for multicomponent equilibrium concurrently. Applying our approach to natural samples from the 2014–2015 Holuhraun lava returns *P–T* estimates in excellent agreement with published values from numerous independent methods: 232±140(1SEE) MPa and 1161±27(1SEE) °C. Our findings illustrate how reliable estimates of storage conditions can be obtained from complex clinopyroxene crystals carried by tholeiitic magmas when sufficiently robust equilibrium filtering is undertaken.

ACKNOWLEDEGMENTS

We thank the 2014–2015 Holuhraun Eruption Team (Institute of Earth Sciences, University of Iceland) for sampling during the eruption. J. Feige prepared samples, R. Balzer and S.A. Linsler assisted with IHPV experiments, and R.A. Almeev and L.A. Fischer assisted with EPMA. We thank Silvio Mollo, Andreas Klügel and one anonymous reviewer for their detailed and constructive reviews that greatly improved our manuscript. We also thank Val Troll for his editorial handling. Most of the 300-MPa experiments initially formed part of an MSc thesis (Hannover) undertaken by A.-S.S. under the supervision of D.A.N. and F.H.

FUNDING

This work and D.A.N. were supported by the Alexander von Humboldt Foundation, the German Research Foundation (NE2097/1-1) and a Presidential Fellowship from the University of Manchester.

FIGURE CAPTIONS

Fig. 1. Map showing the location of the 2014–2015 Holuhraun lava in central Iceland. The extent of the lava flow is shown in red. Black points show the epicentres of earthquakes associated with dyke propagation from the Bárðarbunga central volcano towards the eruption site (Ágústsdóttir *et al.*, 2016). Calderas and central volcanoes are outlined with solid and dashed lines respectively. Sample MSR161014 was collected at the location marked with a black star.

Fig. 2. Photomicrographs of sample MSR161014 from the 2014–2015 Holuhraun lava under (a) plane and (b) crossed polars. Macrocrysts of olivine (ol), plagioclase (plg) and clinopyroxene (cpx) are visible within a crystalline groundmass. The labelled clinopyroxene is in subophitic arrangement with plagioclase and shows sector zoning under crossed polars.

Fig. 3. Backscattered electron (BSE) images of clinopyroxene macrocrysts in sample MSR161014 from the 2014–2015 Holuhraun lava. Olivine (ol) and plagioclase (plg) macrocrysts are indicated. Interpretive sketches are shown to highlight patterns of sector and concentric zoning. Compositional profiles through pairs of sectors measured by electron probe microanalysis (EPMA) are marked on the sketches.

Fig. 4. Backscattered electron (BSE) images of typical products from experiments on sample MSR161014. (a) Olivine (ol), plagioclase (plg) and clinopyroxene (cpx) crystals in a glass (gl) matrix produced at 1160 °C and 300 MPa in a graphite-Pt double capsule. Zoning is highlighted in the largest clinopyroxene crystal. (b) Small, euhedral clinopyroxene crystals produced at 1200 °C and 600 MPa in an AuPd capsule. (c) Large, euhedral clinopyroxene crystals produced at 1180 °C and 300 MPa in a graphite-Pt double capsule. (d) Chains of small clinopyroxene crystals associated with somewhat larger plagioclase crystals produced at 1140 °C and 300 MPa in an AuPd capsule.

Fig. 5. Natural and experimental glass compositions from the 2014–2015 Holuhraun lava. Matrix glass and melt inclusion compositions from Halldórsson *et al.* (2018) and Hartley *et al.* (2018) are shown as dark and light grey circles respectively. Note that published matrix glasses with <6 wt.% MgO preserve an imprint of syn-emplacement crystallisation and are unrepresentative of magmatic liquids at depth (Halldórsson et al., 2018). The experimental starting glass synthesised from sample MSR161014 is shown as a black star. Mean experimental glass compositions produced at different temperatures are shown with coloured symbols. Red symbols indicate experiments in AuPd capsules and blue symbols experiments in graphite-Pt (C-Pt) double capsules. Circles, diamonds and squares indicate glasses produced at 100, 300 and 600 MPa respectively. All Fe is assumed to be Fe^{2+} (i.e. FeO*). Characteristic 2σ analytical uncertainties are shown.

Fig. 6. Summary of natural and experimental olivine (ol) and plagioclase (plg) compositions from the 2014–2015 Holuhraun lava. Mean experimental compositions are shown using the same symbols as in Fig. 5. Core and rim compositions are annotated. Characteristic 2σ analytical uncertainties are shown. (a) Olivine compositions are summarised in terms of their forsterite [X_{Fo}, where X_{Fo} = Mg/(Mg+Fe) on a molar basis] and Mn contents. Olivine macrocryst compositions from Halldórsson *et al.* (2018) are shown as light grey circles; natural compositions from sample MSR161014 are shown as dark grey circles. (b) Plagioclase compositions are summarised in terms of their anorthite [X_{An}, where X_{An} = Ca/(Ca+Na+K) on a molar basis] and K contents. Plagioclase micro- and macrocryst compositions from Halldórsson *et al.* (2018) are shown as outlined white diamonds and light grey circles respectively; compositions from sample MSR161014 are shown as dark grey circles. Experimental plagioclase crystals produced at 600 MPa are more heterogeneous than those produced under other conditions, as reflected in the greater uncertainty shown for this experiment.

Fig. 7. Summary of natural and experimental clinopyroxene (cpx) compositions from the 2014–2015 Holuhraun lava. Clinopyroxene macrocryst compositions from Halldórsson *et al.* (2018) are shown as light grey circles. High-$Mg\#_{cpx}$ clinopyroxene macrocrysts [where $Mg\#_{cpx}$ = Mg/(Mg+Fe) on a molar basis where all Fe is assumed to be Fe^{2+}] are shown as outlined white circles. Compositions from sample MSR141016 are shown as dark grey circles. Mean experimental clinopyroxene compositions are shown using the same symbols as in Fig. 5; see Fig. 10 for more detailed information about variability in experimetnal clinopyroxene compositions. Core and rim compositions are annotated. Characteristic 2σ analytical uncertainties are shown.

Fig. 8. Summary of natural and experimental clinopyroxene (cpx) major element compositions from the 2014–2015 Holuhraun lava. Compositions are expressed as cations calculated on a six-oxygen basis (e.g., Putirka, 2008). Spot analyses from compositional profiles through cpx-21 and cpx-22 (profiles A–A′ and A–A″, and B–B′ and B–B″ respectively; Fig. 3) are shown with circles and diamonds respectively. Low- and high-BSE-intensity sector zones are shown with blue and turquoise symbols respectively. All Fe is assumed to be Fe^{2+} (i.e. Fe*). Mean experimental compositions (n = 16–46) are shown using the same symbols as in Fig. 5; see Fig. 10 for more detailed information. Characteristic 2σ analytical uncertainties are shown.

Fig. 9. Compositional profiles through pairs of sector zones from the 2014–2015 Holuhraun lava. Low-BSE-intensity sectors are shown with dark symbols and high-BSE-intensity sectors with light ones. $Mg\#_{cpx}$ is Mg/(Mg+Fe) on a molar basis where all Fe is assumed to be Fe^{2+}. Diopside-hedenbergite (DiHd), Ca-Tschermak's (CaTs) and jadeite (Jd) component contents were calculated following Putirka (2008). Characteristic 2σ analytical uncertainties are shown. (a) Profiles through low- and high-BSE-intensity sector zones in cpx-21 (profiles A–A′ and A–A″respectively; Fig. 3a). (b) Profiles through low- and high-BSE-intensity sector zones in cpx-22 (profiles B–B′ and B–B″ respectively; Fig. 3b).

Fig. 10. Experimental clinopyroxene compositions from different run temperatures. Mean clinopyroxene compositions from each run are shown using the same symbols as in Fig. 5. Individual spot analyses from clinopyroxene crystals are shown with smaller symbols. Data are shown for the following temperatures: 1140 °C (a, d and g), 1160 °C (b, e and h) and 1180 °C (c, f and i). Natural data are shown using the same symbols as in Fig. 7. Characteristic 2σ analytical uncertainties are shown.

Fig. 11. Mean-normalised standard deviations ($\sigma/\bar{x}$) of clinopyroxene (a) Na_2O and (b) Al_2O_3 contents as functions of melt fraction (*F*). Data are shown using the same symbols as in Fig. 5. Grey horizontal lines show variability in the Kakanui augite standard (NMNH 122142) as an indication of analytical uncertainties. Tie lines join 300-MPa experiments performed at the same temperatures.

Fig. 12. Ferric iron systematics in natural and experimental clinopyroxene crystals. (a) Mean experimental clinopyroxene Fe^{3+} contents estimated following Lindsley (1983) as a function of Mg content. Data are shown using the same symbols as in Fig. 5. (b) Mean clinopyroxene $Fe^{3+}/\Sigma Fe$ values as a function of Mg content. (c and d) Mean clinopyroxene Fe^{3+} contents as functions of (c) Al, (d) Ca and (e) Na contents. Tie lines join 300-MPa experiments performed at the same temperature.

Fig. 13. Pressure (*P*) and temperature (*T*) estimates from experimental clinopyroxene–liquid pairs calculated iteratively with equation 1 of Neave and Putirka (2017) and equation 33 of Putirka (2008). Small symbols show *P*–*T* values calculated from all clinopyroxene analyses. Large symbols show *P*–*T* values calculated from filtered clinopyroxene analyses whose observed diopside-hedenbergite (DiHd), enstatite-ferrosilite (EnFs) and Ca-Tschermak's (CaTs) component contents calculated following Putirka (2008) were within one standard error of estimate (SEE) of values predicted with equations 6 and 7 of Mollo *et al.* (2013) (DiHd and EnFs) and equation 3.4 of Putirka (1999) (CaTs). Kernel density estimates (KDEs) show *P* and

T distributions calculated for both all and filtered subsets clinopyroxene analyses (dashed and solid lines respectively). Mean *P* and *T* estimates from filtered clinopyroxene analyses are shown beside the KDEs; error bars indicate model SEEs. (a) Experiments performed in AuPd capsules at 300 MPa. (b) Experiments performed in AuPd capsules at 600 MPa. (c) Experiments performed in graphite-Pt (C-Pt) double capsules at 100 MPa. (d) Experiments performed in graphite-Pt double capsules at 300 MPa.

Fig. 14. Comparison of observed and predicted diopside-hedenbergite (DiHd) component contents in experimental clinopyroxenes. Observed DiHd component contents were calculated following Putirka (2008). Predicted DiHd component contents were calculated by iteratively solving equations 6 and 7 of Mollo *et al.* (2013) using the *P–T* conditions presented in Fig. 13. One-to-one relationships between observed and predicted DiHd component contents are shown as solid black lines. Model uncertainties (standard errors of estimate) are shown as envelopes delimted by dashed grey lines. (a) Experiments performed in AuPd capsules at 300 MPa. (b) Experiments performed in AuPd capsules at 600 MPa. (c) Experiments performed in graphite-Pt (C-Pt) double capsules at 100 MPa. (d) Experiments performed in graphite-Pt double capsules at 300 MPa.

Fig. 15. Pre-eruptive storage conditions of the 2014–2015 Holuhraun lava estimated with natural clinopyroxene macrocrysts from sample MSR141016. Iterative geothermobarometric calculations were performed using equation 1 of Neave and Putirka (2017) and equation 33 of Putirka (2008). (a) Pressure (*P*) and temperature (*T*) estimates calculated using an iterative melt-matching algorithm adapted from Neave *et al.* (2013) and Neave and Putirka (2017). Putative equilibrium melts were sourced from the matrix glass data of Halldórsson *et al.* (2018). Clinopyroxene–liquid pairs were considered to be in equilibrium when observed diopside-hedenbergite (DiHd), enstatite-ferrosilite (EnFs) and Ca-Tschermak's (CaTs) component contents were within one standard error of estimate (SEE) of values predicted with equations

6 and 7 of Mollo *et al.* (2013) (DiHd and EnFs) and equation 3.4 of Putirka (1999) (CaTs), and observed $K_{D\text{cpx–liq}}^{\text{Mg–Fe}}$ values were within 0.03 of values predicted with equation 35 of Putirka (2008) assuming a melt $Fe^{3+}/\Sigma Fe$ value of 0.15 (Bali *et al.*, 2018). Kernel density estimates (KDEs) showing *P* and *T* distributions are shown alongside mean *P* and *T* values; error bars indicate model SEEs. (b) Storage conditions estimated with the spreadsheet included in the Supplementary Material by pairing clinopyroxene analyses with the mean matrix glass composition of Halldórsson *et al.* (2018) and applying the same equilibrium criteria used in calculations with the melt-matching algorithm. Results with thick outlines are from analyses located within the rims (but not outermost rims) of clinopyroxene macrocrysts most likely to have been in textural equilibrium with their carrier liquids at depth (e.g., Klügel *et al.*, 2005).

Fig. 16. Results of geothermobarometric calculations performed on sector zone pairs from the 2014–2015 Holuhraun lava. Results from low-BSE-intensity sectors are shown with dark symbols and results from high-BSE-intensity sectors with light ones. Dashed lines and small circles show results obtained by pairing all clinopyroxene analyses with the mean matrix glass composition from Halldórsson *et al.* (2018) and applying no filtering. Large circles show the results of calculations with an iterative melt-matching algorithm to which equilibrium filtering was applied (Fig. 15a). Deviations from equilibrium are expressed as differences between observed and predicted diopside-hedenbergite (DiHd), enstatite-ferrosilite (EnFs) and Ca-Tschermak's (CaTs) component contents (i.e. $\Delta_{\text{component}}$ values). DiHd and EnFs component contents were predicted with equations 6 and 7 of Mollo *et al.* (2013) and CaTs component contents with equation 3.4 of Putirka (1999). Jadeite–liquid equilibrium constants are also presented as values of $\ln(K_{\text{Jd–liq}})$. (a) Profiles through low- and high-BSE-intensity sector zones in cpx-21 (profiles A–A′ and A–A″ respectively; Fig. 3a). (b) Profiles through low- and high-BSE-intensity sector zones in cpx-22 (profiles B–B′ and B–B″ respectively; Fig. 3b).

REFERENCES

Ágústsdóttir, T., Woods, J., Greenfield, T., Green, R. G., White, R. S., Brandsdóttir, B., Steinthorsson, S. & Soosalu, H. (2016). Episodic propagation of the 2014 Bárðarbunga-Holuhraun dike intrusion, central Iceland. *Geophysical Research Letters* **43**, 1–9.

Almeev, R. R., Holtz, F., Koepke, J. & Parat, F. (2012). Experimental calibration of the effect of H_2O on plagioclase crystallization in basaltic melt at 200 MPa. *American Mineralogist* **97**, 1234–1240.

Applegarth, L. J., Tuffen, H., James, M. R., Pinkerton, H. & Cashman, K. V. (2013). Direct observations of degassing-induced crystallization in basalts. *Geology* **41**, 243–246.

Baker, M. B. & Grove, T. L. (1985). Kinetic controls on pyroxene nucleation and metastable liquid lines of descent in a basaltic andesite. *American Mineralogist* **70**, 279–287.

Bali, E., Hartley, M. E., Halldórsson, S. A., Guðfinnsson, G. H. & Jakobsson, S. (2018). Melt inclusion constraints on volatile systematics and degassing history of the 2014–2015 Holuhraun eruption, Iceland. *Contributions to Mineralogy and Petrology* **173**, 9.

Balta, J. B., Beckett, J. R. & Asimow, P. D. (2011). Thermodynamic properties of alloys of gold-74/palladium-26 with variable amounts of iron and the use of Au-Pd-Fe alloys as containers for experimental petrology. *American Mineralogist* **96**, 1467–1474.

Barr, J. A. & Grove, T. L. (2010). AuPdFe ternary solution model and applications to understanding the fO_2 of hydrous, high-pressure experiments. *Contributions to Mineralogy and Petrology* **160**, 631–643.

Bennett, S. L., Blundy, J. & Elliott, T. (2004). The effect of sodium and titanium on crystal-melt partitioning of trace elements. *Geochimica et Cosmochimica Acta* **68**, 2335–2347.

Berndt, J., Koepke, J. & Holtz, F. (2005). An experimental investigation of the influence of

water and oxygen fugacity on differentiation of MORB at 200 MPa. *Journal of Petrology* **46**, 135–167.

Berndt, J., Liebske, C., Holtz, F., Freise, M., Nowak, M., Ziegenbein, D., Hurkuck, W. & Koepke, J. (2002). A combined rapid-quench and H_2-membrane setup for internally heated pressure vessels: Description and application for water solubility in basaltic melts. *American Mineralogist* **87**, 1717–1726.

Blundy, J. D., Falloon, T. J., Wood, B. J. & Dalton, J. A. (1995). Sodium partitioning between clinopyroxene and silicate melts. *Journal of Geophysical Research: Solid Earth* **100**, 15501–15515.

Bonny, E., Thordarson, T., Wright, R., Höskuldsson, A. & Jónsdóttir, I. (2018). The Volume of Lava Erupted during the 2014 to 2015 Eruption at Holuhraun, Iceland: a Comparison between Satellite- and Ground-Based Measurements. *Journal of Geophysical Research: Solid Earth* **123**, 1–15.

Borisov, A., Behrens, H. & Holtz, F. (2018). Ferric/ferrous ratio in silicate melts: a new model for 1 atm data with special emphasis on the effects of melt composition. *Contributions to Mineralogy and Petrology* **173**, 98.

Botcharnikov, R. E., Koepke, J., Holtz, F., McCammon, C. & Wilke, M. (2005). The effect of water activity on the oxidation and structural state of Fe in a ferro-basaltic melt. *Geochimica et Cosmochimica Acta* **69**, 5071–5085.

Bryan, W. B. (1983). Systematics of modal phenocryst assemblages in submarine basalts: Petrologic implications. *Contributions to Mineralogy and Petrology* **83**, 62–74.

Carlson, R. L. & Herrick, C. N. (1990). Densities and porosities in the oceanic crust and their variations with depth and age. *Journal of Geophysical Research* **95**, 9153–9170.

Cashman, K. V. (1993). Relationship between plagioclase crystallization and cooling rate in

basaltic melts. *Contributions to Mineralogy and Petrology* **113**, 126–142.

Couch, S., Sparks, R. S. J. & Carroll, M. R. (2001). Mineral disequilibrium in lavas explained by convective self-mixing in open magma chambers. *Nature* **411**, 1037–1039.

Downes, M. J. (1974). Sector and oscillatory zoning in calcic augites from M. Etna, Sicily. *Contributions to Mineralogy and Petrology* **47**, 187–196.

Dowty, E. (1976). Crystal structure and crystal growth: II. sector zoning in minerals. *American Mineralogist* **61**, 460–469.

Erdmann, M. & Koepke, J. (2016). Experimental temperature cycling as a powerful tool to enlarge melt pools and crystals at magma storage conditions. *American Mineralogist* **101**, 960–969.

Gaetani, G. A. & Grove, T. L. (1998). The influence of water on melting of mantle peridotite. *Contributions to Mineralogy and Petrology* **131**, 323–346.

Ginibre, C., Wörner, G. & Kronz, A. (2002). Minor- and trace-element zoning in plagioclase: implications for magma chamber processes at Parinacota volcano, northern Chile. *Contributions to Mineralogy and Petrology* **143**, 300–315.

Green, E. C. R., Holland, T. J. B., Powell, R. & White, R. W. (2012). Garnet and spinel lherzolite assemblages in $MgO–Al_2O_3–SiO_2$ and $CaO–MgO–Al_2O_3–SiO_2$: Thermodynamic models and an experimental conflict. *Journal of Metamorphic Geology* **30**, 561–577.

Grove, T. L. (1981). Use of FePt alloys to eliminate the iron loss problem in 1 atmosphere gas mixing experiments: Theoretical and practical considerations. *Contributions to Mineralogy and Petrology* **78**, 298–304.

Grove, T. L. & Bence, A. E. (1977). Experimental study of pyroxene-liquid interaction in

quartz-normative basalt 15597. *Proceedings of the Lunar Science Conference 8*. Houston, 1549–1579.

Grove, T. L. & Bryan, W. B. (1983). Fractionation of pyroxene-phyric MORB at low pressure: An experimental study. *Contributions to Mineralogy and Petrology* **84**, 293–309.

Grove, T. L. & Juster, T. C. (1989). Experimental investigations of low-Ca pyroxene stability and olivine-pyroxene-liquid equilibria at 1-atm in natural basaltic and andesitic liquids. *Contributions to Mineralogy and Petrology* **103**, 287–305.

Grove, T. L., Kinzler, R. J. & Bryan, W. B. (1992). Fractionation of Mid-Ocean Ridge Basalt (MORB). *Mantle Flow and Melt Generation at Mid-Ocean Ridges, Geophysical Monograph 71*. Washington D.C.: American Geophysical Union, 281–310.

Guðmundsson, M. T. *et al.* (2016). Gradual caldera collapse at Bárdarbunga volcano, Iceland, regulated by lateral magma outflow. *Science* **353**, aaf8988.

Halldórsson, S. A., Bali, E., Hartley, M. E., Neave, D. A., Peate, D. W., Guðfinnsson, G. H., Bindeman, I. N. & Whitehouse, M. J. (2018). Petrology and geochemistry of the 2014–2015 Holuhraun eruption, central Iceland: compositional and mineralogical characteristics, temporal variability and magma storage. *Contributions to Mineralogy and Petrology* **173**, 64.

Halldórsson, S. A., Óskarsson, N., Grönvold, K., Sigurdsson, G., Sverrisdottir, G. & Steinthórsson, S. (2008). Isotopic-heterogeneity of the Thjorsa lava-Implications for mantle sources and crustal processes within the Eastern Rift Zone, Iceland. *Chemical Geology* **255**, 305–316.

Hammer, J. E. (2008). Experimental Studies of the Kinetics and Energetics of Magma Crystallization. *Reviews in Mineralogy and Geochemistry* **69**, 9–59.

Hammer, J. E., Jacob, S., Welsch, B., Hellebrand, E. & Sinton, J. M. (2016). Clinopyroxene in postshield Haleakala ankaramite 1. Efficacy of thermobarometry. *Contributions to Mineralogy and Petrology* **171**, 7.

Hansen, H. & Grönvold, K. (2000). Plagioclase ultraphyric basalts in Iceland: The mush of the rift. *Journal of Volcanology and Geothermal Research* **98**, 1–32.

Hartley, M. E., Bali, E., Maclennan, J., Neave, D. A. & Halldórsson, S. A. (2018). Melt inclusion constraints on petrogenesis of the 2014–2015 Holuhraun eruption, Iceland. *Contributions to Mineralogy and Petrology* **173**, 10.

Hartley, M. E., Morgan, D. J., Maclennan, J., Edmonds, M. & Thordarson, T. (2016). Tracking timescales of short-term precursors to large basaltic fissure eruptions through Fe-Mg diffusion in olivine. *Earth and Planetary Science Letters* **439**, 58–70.

Hartley, M. E., Neave, D. A., Maclennan, J., Edmonds, M. & Thordarson, T. (2015). Diffusive over-hydration of olivine-hosted melt inclusions. *Earth and Planetary Science Letters* **425**, 168–178.

Hildner, E., Klügel, A. & Hansteen, T. H. (2012). Barometry of lavas from the 1951 eruption of Fogo, Cape Verde Islands: Implications for historic and prehistoric magma plumbing systems. *Journal of Volcanology and Geothermal Research* **217–218**, 73–90.

Hollister, L. S. & Gancarz, A. . (1971). Compositional sector-zoning in clinopyroxene from the Narce area, Italy. *American Mineralogist* **56**, 959–979.

Holloway, J. R., Pan, V. & Guðmundsson, G. B. (1992). High-pressure fluid-absent melting experiments in the presence of graphite: oxygen fugacity, ferric/ferrous ratio and dissolved CO_2. *European Journal of Mineralogy* **4**, 105–114.

Holness, M. B., Stock, M. J. & Geist, D. (2019). Magma chambers versus mush zones: constraining the architecture of sub-volcanic plumbing systems from microstructural

analysis of crystalline enclaves. *Philosophical Transactions of the Royal Society A* **377**, 1–28.

Husen, A., Almeev, R. R. & Holtz, F. (2016). The Effect of H_2O and Pressure on Multiple Saturation and Liquid Lines of Descent in Basalt from the Shatsky Rise. *Journal of Petrology* **57**, 309–344.

Jakobsson, S. & Óskarsson, N. (1994). The system C-O in equilibrium with graphite at high pressure and temperature: An experimental study. *Geochimica et Cosmochimica Acta* **58**, 9–17.

Jarosewich, E., Gooley, R. & Husler, J. (1987). Chromium Augite - A New Microprobe Reference Sample. *Geostandards and Geoanalytical Research* **11**, 197–198.

Jarosewich, E., Nelen, J. A. & Norberg, J. A. (1980). Reference samples for electron microprobe analysis. *Geostandards Newsletter* **4**, 43–47.

Kelley, K. A. & Cottrell, E. (2012). The influence of magmatic differentiation on the oxidation state of Fe in a basaltic arc magma. *Earth and Planetary Science Letters* **329–330**, 109–121.

Kirkpatrick, R. J. (1976). Towards a kinetic model for the crystallization of magma bodies. *Journal of Geophysical Research* **81**, 2565–2571.

Klügel, A., Hansteen, T. H. & Galipp, K. (2005). Magma storage and underplating beneath Cumbre Vieja volcano, La Palma (Canary Islands). *Earth and Planetary Science Letters* **236**, 211–226.

Kouchi, A., Sugawara, Y., Kashima, K. & Sunagawa, I. (1983). Laboratory growth of sector zones clinopyroxenes in the system $CaMgSi_2O_6$ – $CaTiAl_2O_6$. *Contributions to Mineralogy and Petrology* **83**, 177–184.

Kress, V. C. & Carmichael, I. S. E. (1991). The compressibility of silicate liquids containing Fe_2O_3 and the effect of composition, temperature, oxygen fugacity and pressure on their redox states. *Contributions to Mineralogy and Petrology* **108**, 82–92.

Leung, I. S. (1974). Sector-zoned Titanaugites: Morphology, Crystal Chemistry, and Growth. *American Mineralogist* **59**, 127–138.

Lindsley, D. H. (1983). Pyroxene thermometry. *American Mineralogist* **68**, 477–493.

Lofgren, G. E., Huss, G. R. & Wasserburg, G. J. (2006). An experimental study of trace-element partitioning between Ti-Al-clinopyroxene and melt: Equilibrium and kinetic effects including sector zoning. *American Mineralogist* **91**, 1596–1606.

Longpré, M.-A., Klügel, A., Diehl, A. & Stix, J. (2014). Mixing in mantle magma reservoirs prior to and during the 2011–2012 eruption at El Hierro, Canary Islands. *Geology* **42**, 315–318.

Longpré, M.-A., Stix, J., Klügel, A. & Shimizu, N. (2017). Mantle to surface degassing of carbon- and sulphur-rich alkaline magma at El Hierro, Canary Islands. *Earth and Planetary Science Letters* **460**, 268–280.

Luth, R. W. & Canil, D. (1993). Ferric iron in mantle-derived pyroxenes and a new oxybarometer for the mantle. *Contributions to Mineralogy and Petrology* **113**, 236–248.

Maclennan, J., McKenzie, D., Grönvold, K. & Slater, L. (2001). Crustal accretion under Northern Iceland. *Earth and Planetary Science Letters* **191**, 295–310.

McGuire, A. V., Dyar, M. D. & Ward, K. A. (1989). Neglected Fe^{3+}/Fe^{2+} ratios – a study of Fe^{3+} content of megacrysts from alkali basalts. *Geology* **17**, 687–690.

Médard, E., McCammon, C. A., Barr, J. A. & Grove, T. L. (2008). Oxygen fugacity, temperature reproducibility, and H_2O contents of nominally anhydrous piston-cylinder

experiments using graphite capsules. *American Mineralogist* **93**, 1838–1844.

Mollo, S. *et al.* (2018). An integrated P-T-H_2O-lattice strain model to quantify the role of clinopyroxene fractionation on REE+Y/HFSE patterns of mafic alkaline magmas: Application to eruptions at Mt. Etna. *Earth-Science Reviews* **185**, 32–56.

Mollo, S., Del Gaudio, P., Ventura, G., Iezzi, G. & Scarlato, P. (2010). Dependence of clinopyroxene composition on cooling rate in basaltic magmas: Implications for thermobarometry. *Lithos* **118**, 302–312.

Mollo, S. & Hammer, J. E. (2017). Dynamic crystallization in magmas. *Mineral reaction kinetics: Microstructures, textures, chemical and isotopic signatures*. European Mineralogical Union and Mineralogical Society of Great Britain and Ireland: EMU Notes in Mineralogy 16, 378–418.

Mollo, S., Lanzafame, G., Masotta, M., Iezzi, G., Ferlito, C. & Scarlato, P. (2011). Cooling history of a dike as revealed by mineral chemistry: A case study from Mt. Etna volcano. *Chemical Geology* **288**, 39–52.

Mollo, S., Putirka, K. D., Misiti, V., Soligo, M. & Scarlato, P. (2013). A new test for equilibrium based on clinopyroxene-melt pairs: Clues on the solidification temperatures of Etnean alkaline melts at post-eruptive conditions. *Chemical Geology* **352**, 92–100.

Morimoto, N., Fabries, J., Ferguson, A. K., Ginzburg, I. V., Ross, M., Seifert, F. A., Zussman, J., Aoki, K. & Gottardi, G. (1988). Nomenclature of pyroxenes. *American Mineralogist* **73**, 1123–1133.

Nakamura, Y. (1973). Origin of sector-zoning of igneous clinopyroxenes. *American Mineralogist* **58**, 986–990.

Nakamura, Y. & Coombs, D. S. (1973). Clinopyroxenes in the tawhiroko tholeiitic dolerite at Moeraki, north-eastern Otago, New Zealand. *Contributions to Mineralogy and*

Petrology **42**, 213–228.

Namur, O., Charlier, B., Toplis, M. J. & Vander Auwera, J. (2012). Prediction of plagioclase-melt equilibria in anhydrous silicate melts at 1-atm. *Contributions to Mineralogy and Petrology* **163**, 133–150.

Neave, D. A., Maclennan, J., Hartley, M. E., Edmonds, M. & Thordarson, T. (2014). Crystal storage and transfer in basaltic systems: the Skuggafjöll eruption, Iceland. *Journal of Petrology* **55**, 2311–2346.

Neave, D. A., Maclennan, J., Thordarson, T. & Hartley, M. E. (2015). The evolution and storage of primitive melts in the Eastern Volcanic Zone of Iceland: the 10 ka Grímsvötn tephra series (i.e. the Saksunarvatn ash). *Contributions to Mineralogy and Petrology* **170**, 21.

Neave, D. A., Passmore, E., Maclennan, J., Fitton, J. G. & Thordarson, T. (2013). Crystal-melt relationships and the record of deep mixing and crystallization in the AD 1783 Laki eruption, Iceland. *Journal of Petrology* **54**, 1661–1690.

Neave, D. A. & Putirka, K. D. (2017). A new clinopyroxene-liquid barometer, and implications for magma storage pressures under Icelandic rift zones. *American Mineralogist* **102**, 777–794.

Pankhurst, M. J., Morgan, D. J., Thordarson, T. & Loughlin, S. C. (2018). Magmatic crystal records in time, space, and process, causatively linked with volcanic unrest. *Earth and Planetary Science Letters* **493**, 231–241.

Passmore, E., Maclennan, J., Fitton, J. G. & Thordarson, T. (2012). Mush disaggregation in basaltic magma chambers: Evidence from the AD 1783 Laki eruption. *Journal of Petrology* **53**, 2593–2623.

Pedersen, G. B. M. *et al.* (2017). Lava field evolution and emplacement dynamics of the

2014–2015 basaltic fissure eruption at Holuhraun, Iceland. *Journal of Volcanology and Geothermal Research* **340**, 155–169.

Petrone, C. M., Bugatti, G., Braschi, E. & Tommasini, S. (2016). Pre-eruptive magmatic processes re-timed using a non-isothermal approach to magma chamber dynamics. *Nature Communications* **7**, 12946.

Putirka, K. D. (1999). Clinopyroxene + liquid equilibria to 100 kbar and 2450 K. *Contributions to Mineralogy and Petrology* **135**, 151–163.

Putirka, K. D. (2008). Thermometers and Barometers for Volcanic Systems. *Reviews in Mineralogy and Geochemistry* **69**, 61–120.

Putirka, K. D., Johnson, M., Kinzler, R. J., Longhi, J. & Walker, D. (1996). Thermobarometry of mafic igneous rocks based on clinopyroxene-liquid equilibria, 0–30 kbar. *Contributions to Mineralogy and Petrology* **123**, 92–108.

Sack, R. O. & Ghiorso, M. S. (1994). Thermodynamics of multicomponent pyroxenes: I. Formulation of a general model. *Contributions to Mineralogy and Petrology* **116**, 277–286.

Schuessler, J. A., Botcharnikov, R. E., Behrens, H., Misiti, V. & Freda, C. (2008). Oxidation state of iron in hydrous phono-tephritic melts. *American Mineralogist* **93**, 1493–1504.

Shane, P. & Coote, A. (2018). Thermobarometry of Whangarei volcanic field lavas, New Zealand: Constraints on plumbing systems of small monogenetic basalt volcanoes. *Journal of Volcanology and Geothermal Research* **354**, 130–139.

Shishkina, T. A., Botcharnikov, R. E., Holtz, F., Almeev, R. R. & Portnyagin, M. V. (2010). Solubility of H2O- and CO2-bearing fluids in tholeiitic basalts at pressures up to 500 MPa. *Chemical Geology* **277**, 115–125.

Sigmundsson, F. *et al.* (2015). Segmented lateral dyke growth in a rifting event at Bárðarbunga volcanic system, Iceland. *Nature* **517**, 191–195.

Skulski, T., Minarik, W. & Watson, E. B. (1994). High-pressure experimental trace-element partitioning between clinopyroxene and basaltic melts. *Chemical Geology* **117**, 127–147.

Strong, D. F. (1969). Formation of the hour-glass structure in augite. *Mineralogical Magazine* **37**, 472–479.

Thomson, A. & Maclennan, J. (2013). The distribution of olivine compositions in icelandic basalts and picrites. *Journal of Petrology* **54**, 745–768.

Thordarson, T. & Self, S. (1993). The Laki (Skaftár Fires) and Grímsvötn eruptions in 1783–1785. *Bulletin of Volcanology* **55**, 233–263.

Toplis, M. J. (2005). The thermodynamics of iron and magnesium partitioning between olivine and liquid: Criteria for assessing and predicting equilibrium in natural and experimental systems. *Contributions to Mineralogy and Petrology* **149**, 22–39.

Tormey, D. R., Grove, T. L. & Bryan, W. B. (1987). Experimental petrology of normal MORB near the Kane Fracture Zone: 22°–25°N, mid-Atlantic ridge. *Contributions to Mineralogy and Petrology* **96**, 121–139.

Ubide, T. & Kamber, B. S. (2018). Volcanic crystals as time capsules of eruption history. *Nature Communications* **9**, 326.

Ubide, T., Mollo, S., Zhao, J.-X., Nazzari, M. & Scarlato, P. (2019). Sector-zoned clinopyroxene as a recorder of magma history, eruption triggers, and ascent rates. *Geochimica et Cosmochimica Acta* **251**, 265–283.

Ulmer, P., Kägi, R. & Müntener, O. (2018). Experimentally derived intermediate to silica-rich arc magmas by fractional and equilibrium crystallization at 1.0 GPa: An evaluation

of phase relationships, compositions, liquid lines of descent and oxygen fugacity. *Journal of Petrology* **59**, 11–58.

Villiger, S., Ulmer, P., Müntener, O. & Thompson, A. B. (2004). The Liquid Line of Descent of Anhydrous, Mantle-derived, Tholeiitic Liquids by Fractional and Equilibrium Crystallization—An Experimental Study at 1.0 GPa. *Journal of Petrology* **45**, 2369–2388.

Weis, F. A., Skogby, H., Troll, V. R., Deegan, F. M. & Dahren, B. (2015). Magmatic water contents determined through clinopyroxene: Examples from the Western Canary Islands, Spain. *Geochemistry, Geophysics, Geosystems* **16**, 2127–2146.

Welsch, B., Hammer, J. E., Baronnet, A., Jacob, S., Hellebrand, E. & Sinton, J. M. (2016). Clinopyroxene in postshield Haleakala ankaramite 2. Texture, compositional zoning, and supersaturation in the magma. *Contributions to Mineralogy and Petrology* **171**, 6.

Whitaker, M. L., Nekvasil, H., Lindsley, D. H. & Difrancesco, N. J. (2007). The role of pressure in producing compositional diversity in intraplate basaltic magmas. *Journal of Petrology* **48**, 365–393.

Winpenny, B. & Maclennan, J. (2011). A partial record of mixing of mantle melts preserved in Icelandic phenocrysts. *Journal of Petrology* **52**, 1791–1812.

Zhang, Y., Ni, H. & Chen, Y. (2010). Diffusion data in silicate melts. *Reviews in Mineralogy and Geochemistry* **72**, 311–408.

Table 1 Summary of experimental conditions

Experiment number	P (MPa)	T (°C)	Capsule	Duration (hours)	Fe loss/ gain (%)	fO_2 estimates[1]				H_2O (wt.%)[6]	Phase proportions[7]				ΔT_{cpx}[8] (°C)
						ΔQFM (S08)[2]	ΔQFM (BG10)[3]	ΔQFM (T05)[4]	ΔQFM (B05)[5]		gl	ol	plg	cpx	
synthesis		1600		1+1											
B0188-3	100	1140	AuPd	120	-14		0.51		2.70	1.06	1.00				
Y0185-11	100	1160	AuPd	120	-9	1.29	0.76		2.08	0.75	1.00				
Y0186-2	100	1180	AuPd	72	-1	1.47	1.12		1.76	0.61	1.00				
Y0187-5	100	1200	AuPd	48	6	1.51	1.03		1.44	0.50	1.00				
Y0205-2	300	1140	AuPd	72	3		1.42				0.65		0.15	0.20	20–40
Y0201-2	300	1160	AuPd	75	1		0.77				0.94			0.06	<20
Y0174-7	300	1180	AuPd	90	1	1.55	1.09		1.28	0.64	1.00				
Y0166-10	300	1200	AuPd	48	-6	1.77	0.80		1.38	0.68	1.00				
B0187-8	600	1140	AuPd	96	-9		0.82				0.64		0.10	0.26	>60
B0183-4	600	1160	AuPd	96	-14		0.33				0.87			0.13	>40
B0167-1	600	1180	AuPd	72	-6		0.67				0.90			0.10	>20
B0184-10	600	1200	AuPd	48	-6		0.62				0.99			0.01	>0
Y0272-1	100	1140	C-Pt	96	-3			-0.70			0.66	0.04	0.18	0.12	20–40
Y0287-1	100	1160	C-Pt	72	1			-0.96			0.82	0.02	0.10	0.06	<20
Y0281-1	100	1180	C-Pt	72	-1				-2.72	0.04	1.00				
Y0204-3	300	1140	C-Pt	72	-1			-1.00			0.50	0.00	0.24	0.26	40–60
Y0200-3	300	1160	C-Pt	72	1						0.66		0.15	0.18	20–40
Y0206-3	300	1180	C-Pt	72	0						0.97			0.03	<20
Y0216-3	300	1200	C-Pt	71	-3				-2.08	0.08	1.00				
Y0218-3	300	1220	C-Pt	66	-1				-2.08	0.08	1.00				

[1]Note that all methods of fO_2 estimation used are associated with uncertainties in the order of 0.5-1.0 log units.
[2]Oxygen fugacity estimated by colorimetry following Schuessler *et al.* (2008).
[3]Oxygen fugacity estimated from AuPd-capsule compositions following Barr and Grove (2010).
[4]Oxygen fugacity estimated from glass $Fe^{3+}/\Sigma Fe$ contents determined using $K_{D_{ol-liq}}^{Mg-Fe}$ values calculated following Toplis (2005).
[5]Oxygen fugacity estimated from aH_2O following Botcharnikov *et al.* (2005).
[6]Glass H_2O contents determined by FTIR on superliquidus runs.
[7]gl, glass; ol, olivine; plg, plagioclase; cpx, clinopyroxene. phase proportion rounded to two significant figures.
[8]Difference between experimental T and clinopyroxene liquidus T (i.e. degree of undercooling *sensu lato*).

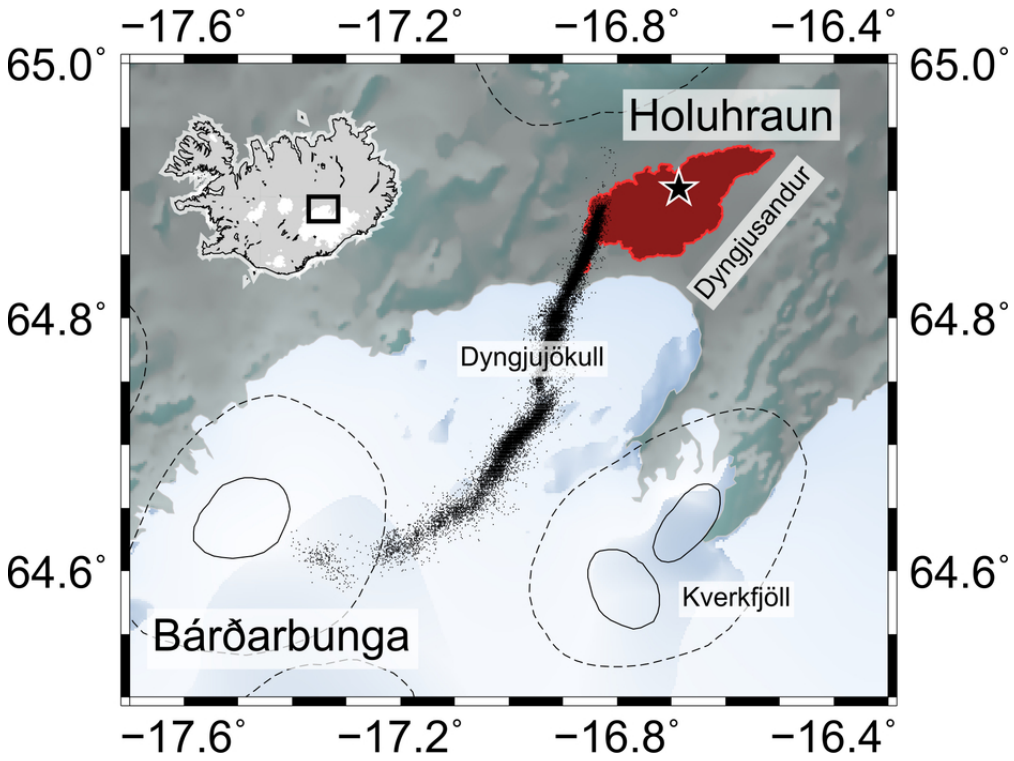

Fig. 1

79x58mm (300 x 300 DPI)

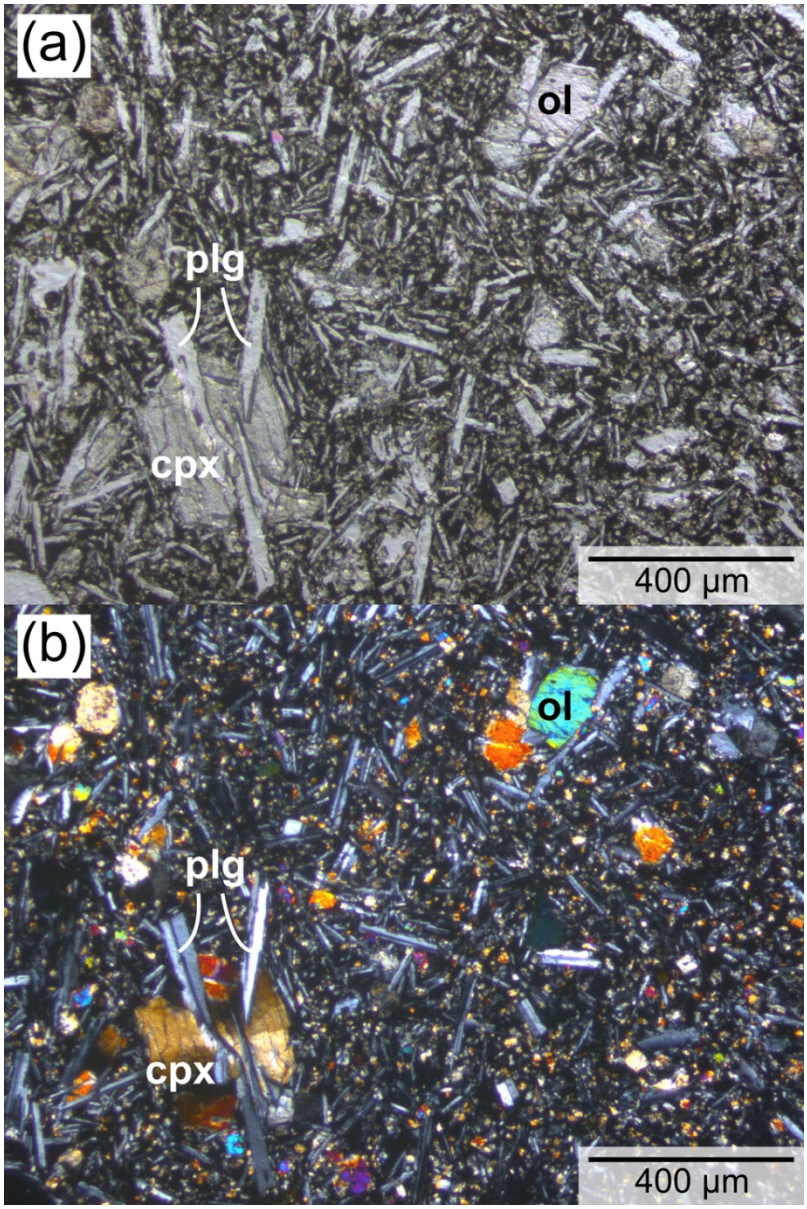

Fig. 2

82x123mm (300 x 300 DPI)

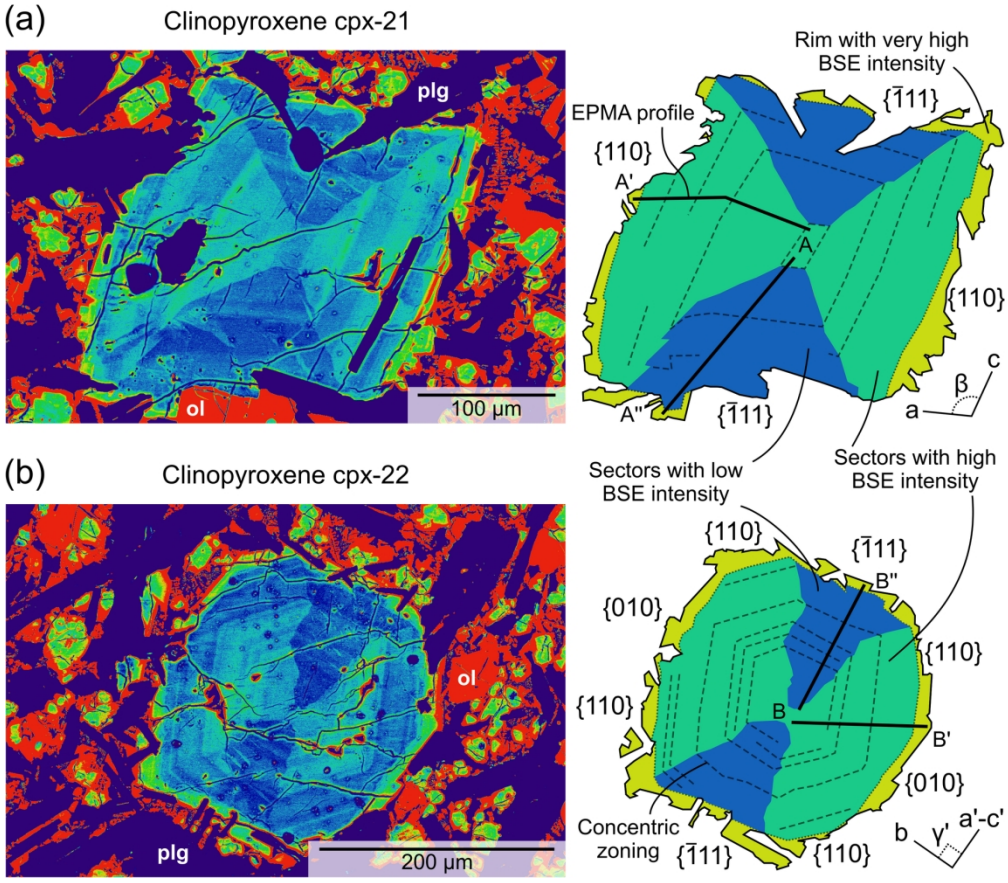

Fig. 3

165x145mm (300 x 300 DPI)

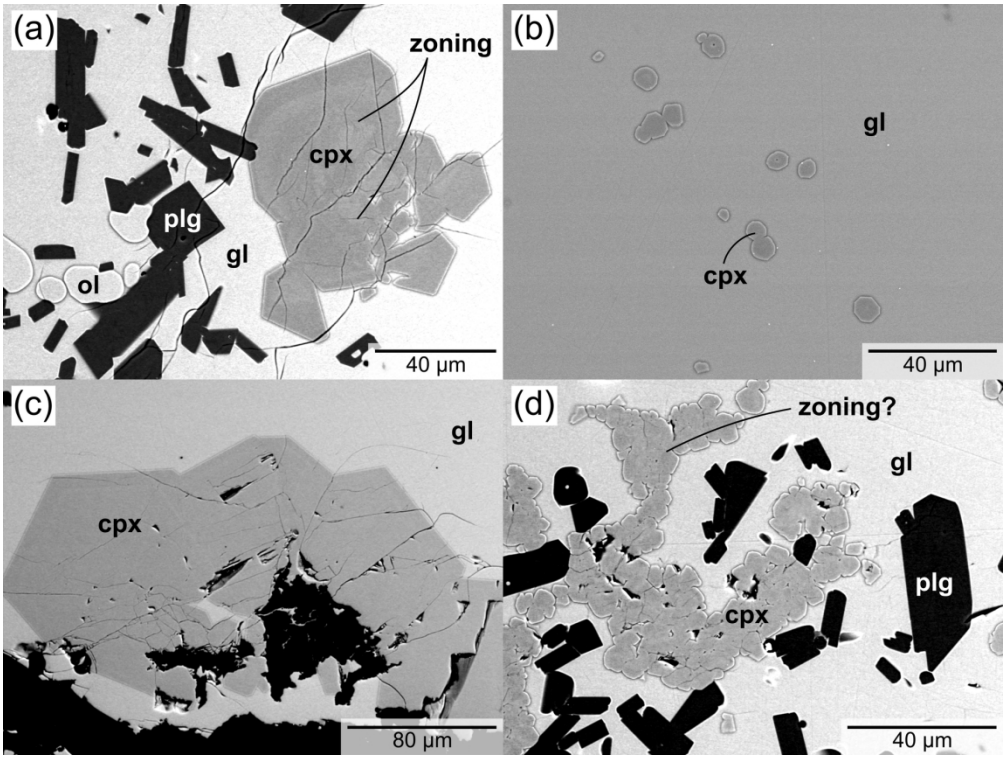

Fig. 4

165x123mm (300 x 300 DPI)

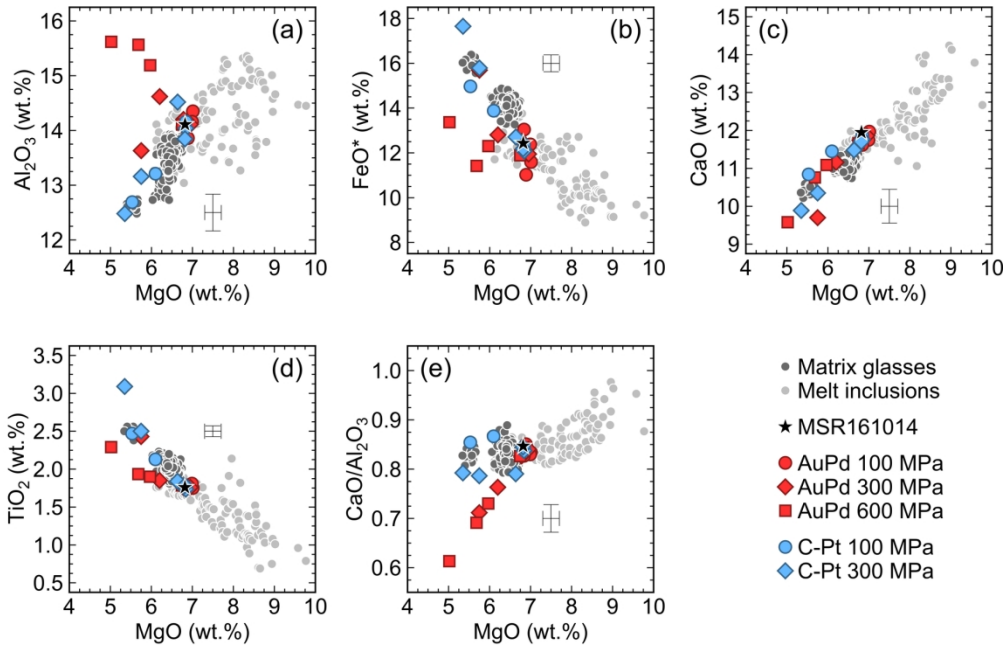

Fig. 5

162x103mm (300 x 300 DPI)

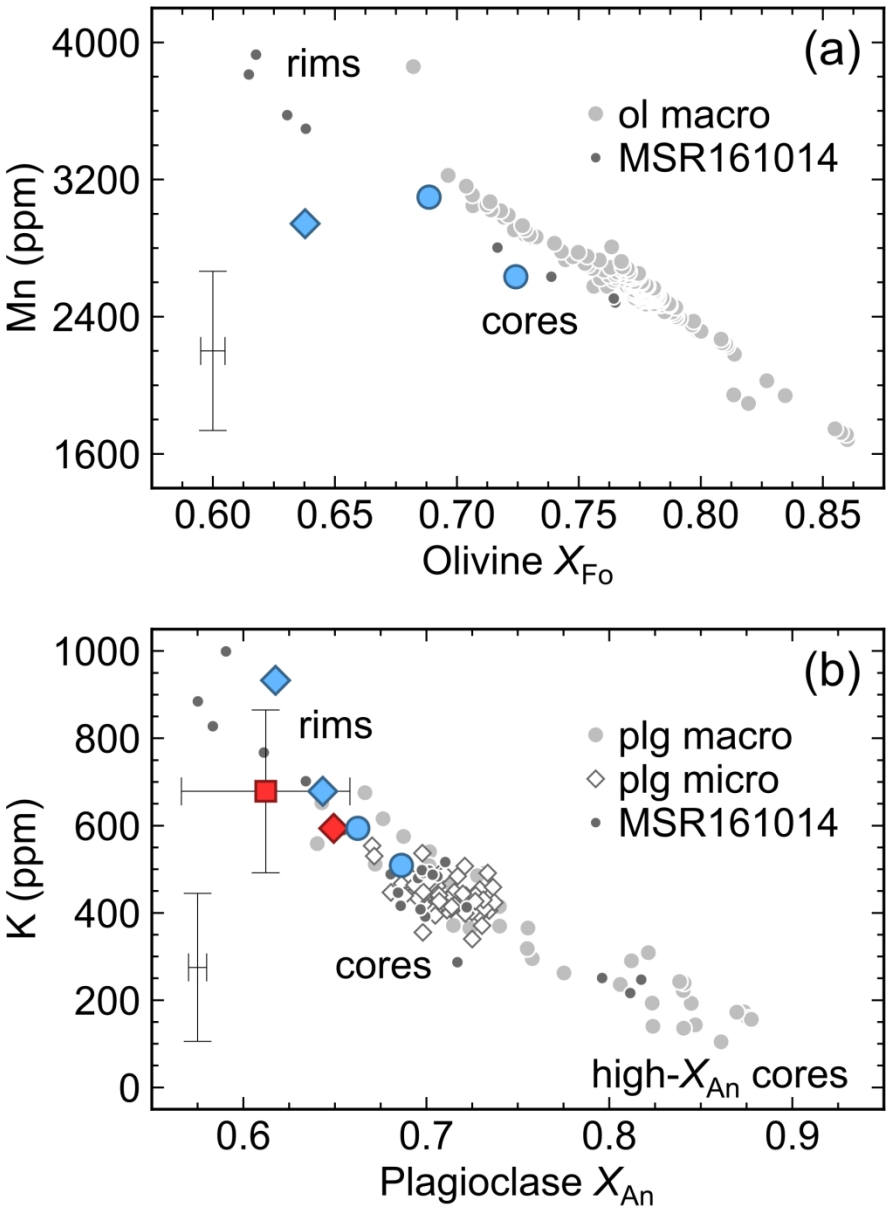
(a)
rims
ol macro
MSR161014
cores
Mn (ppm)
4000
3200
2400
1600
0.60
0.65
0.70
0.75
0.80
0.85
Olivine X_{Fo}
(b)
rims
plg macro
plg micro
MSR161014
cores
high-X_{An} cores
K (ppm)
1000
800
600
400
200
0
0.6
0.7
0.8
0.9
Plagioclase X_{An}

Fig. 6

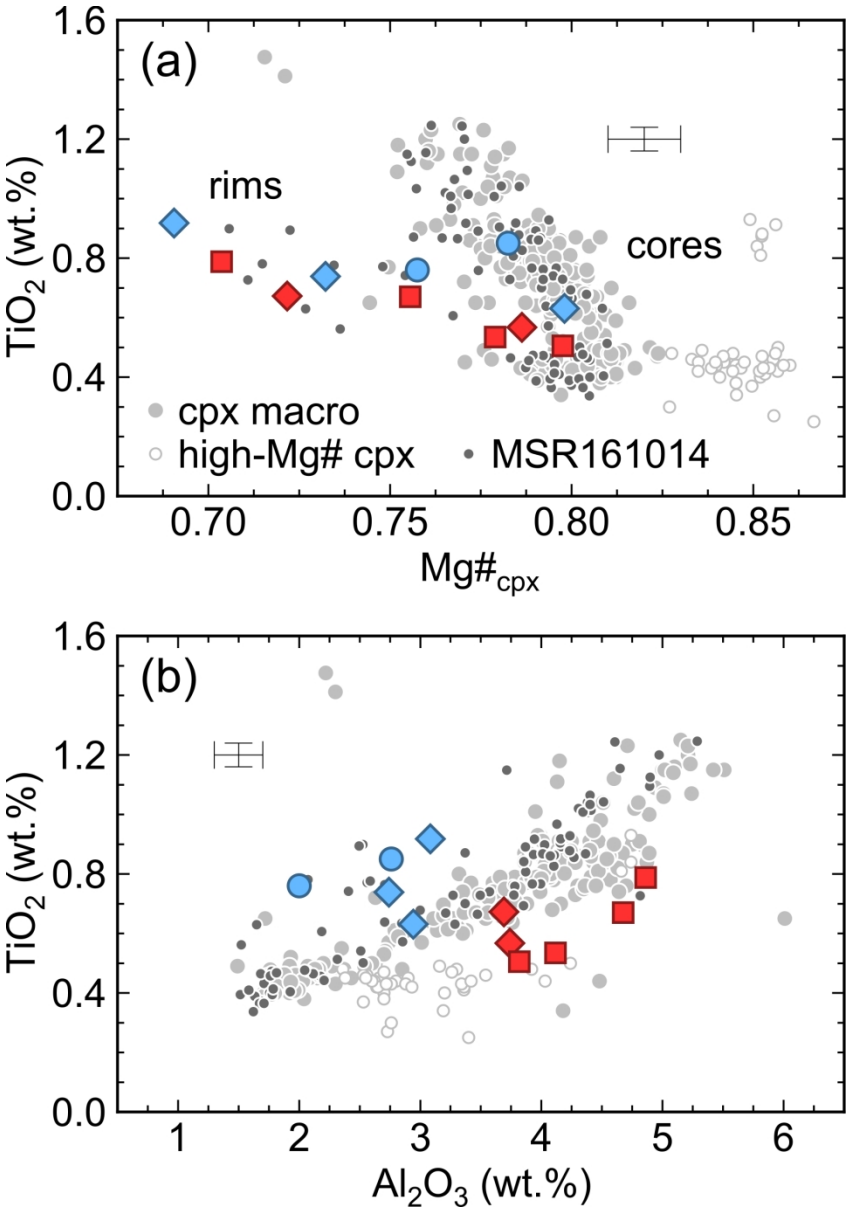
(a)
rims
cores
cpx macro
high-Mg# cpx
MSR161014
TiO2 (wt.%)
Mg#cpx
(b)
TiO2 (wt.%)
Al2O3 (wt.%)

Fig. 7

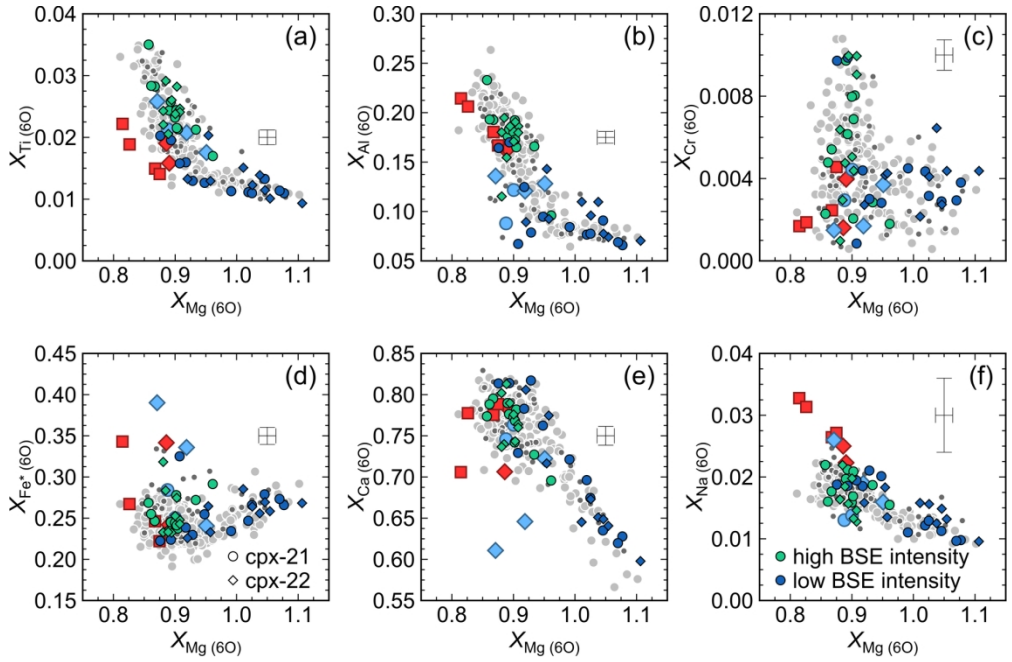

Fig. 8

162x105mm (300 x 300 DPI)

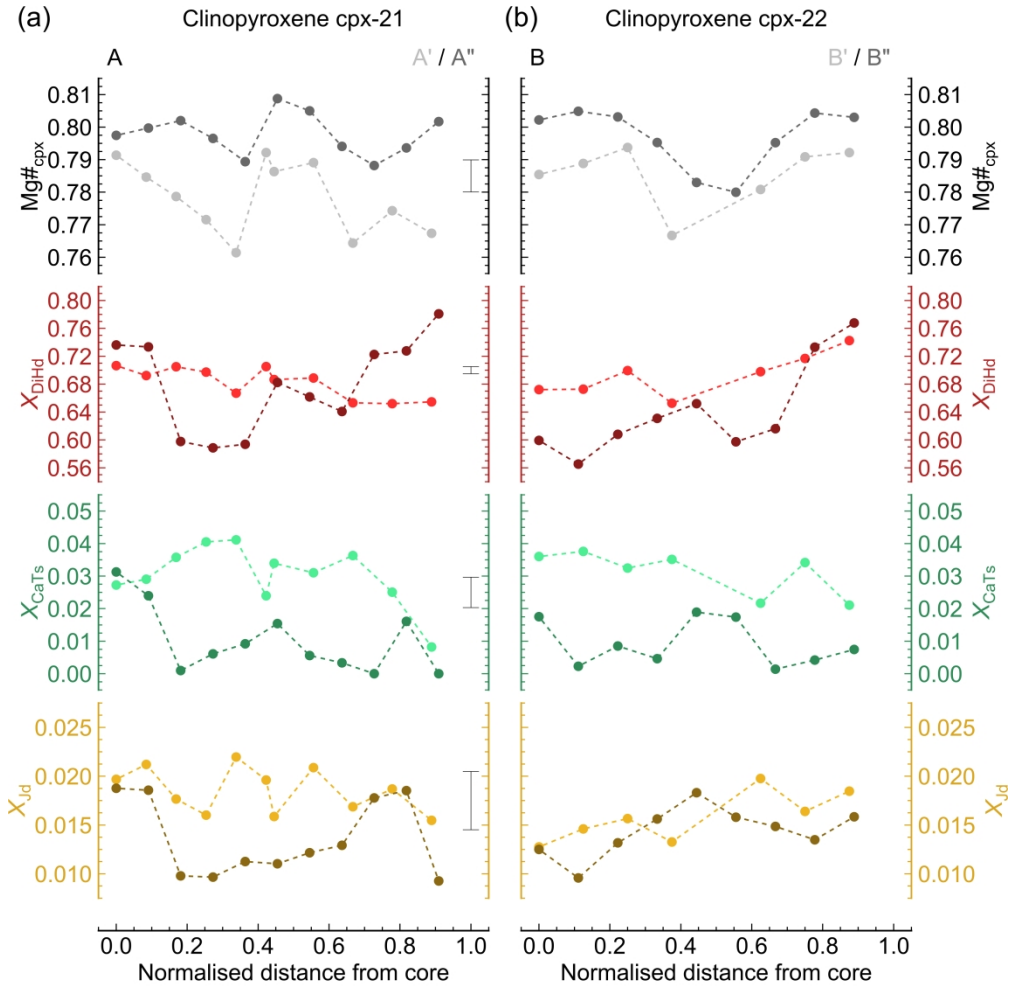
(a)
Clinopyroxene cpx-21
A
A' / A"
(b)
Clinopyroxene cpx-22
B
B' / B"
Mg#cpx
XDiHd
XCaTs
XJd
Normalised distance from core
Normalised distance from core

Fig. 9

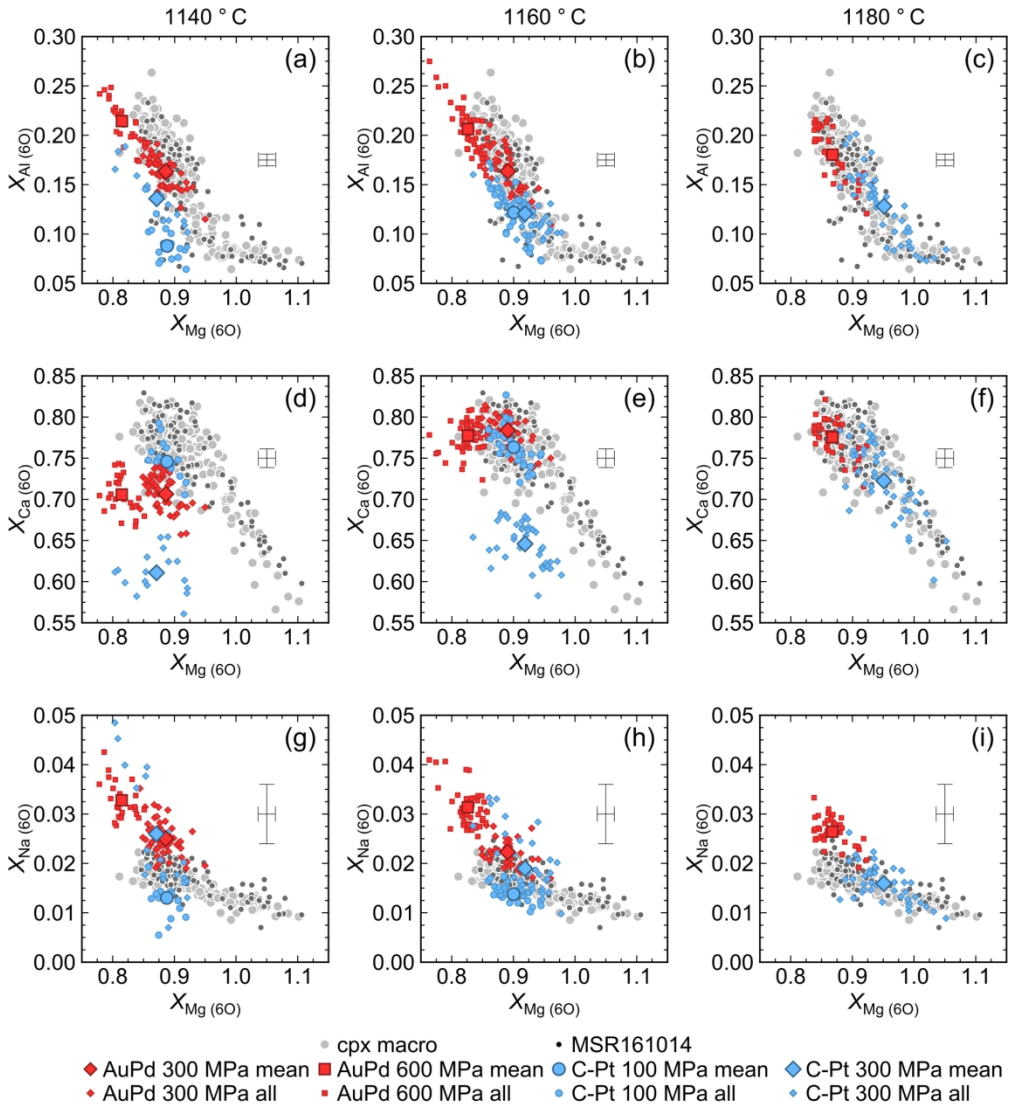

Fig. 10

162x178mm (300 x 300 DPI)

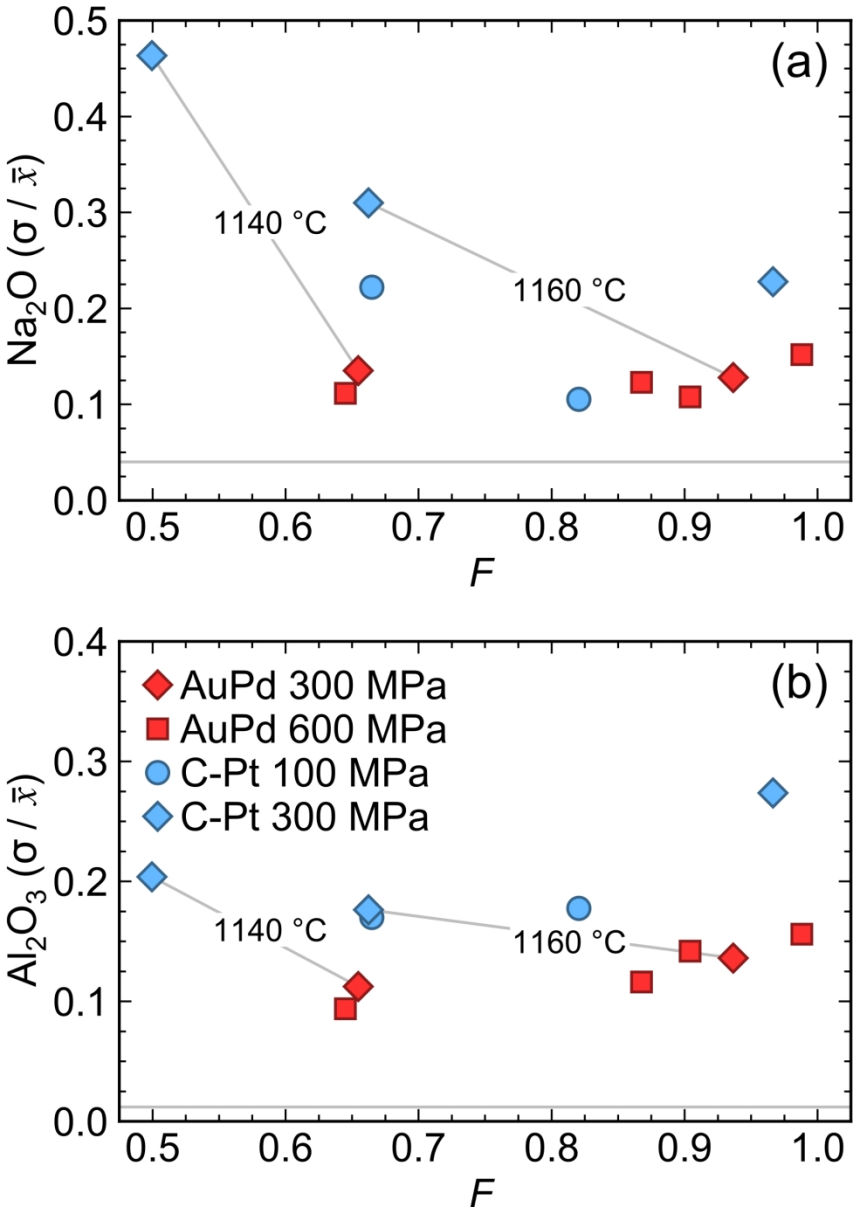
(a)
Na_2O (σ / $\bar{x}$)
1140 °C
1160 °C
F
(b)
AuPd 300 MPa
AuPd 600 MPa
C-Pt 100 MPa
C-Pt 300 MPa
Al_2O_3 (σ / $\bar{x}$)
1140 °C
1160 °C
F

Fig. 11

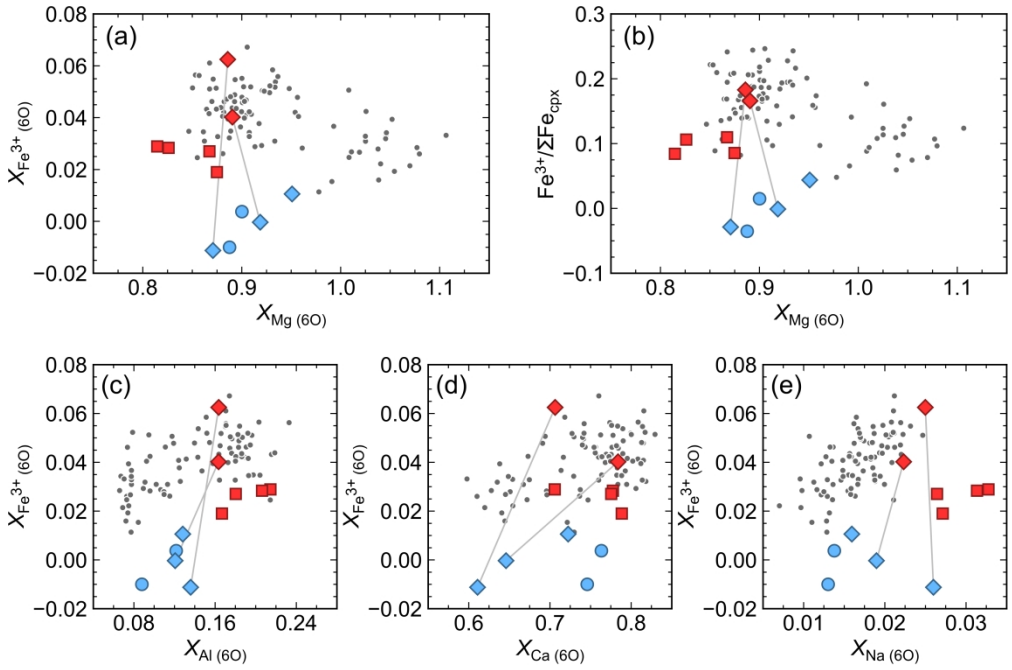

Fig. 12

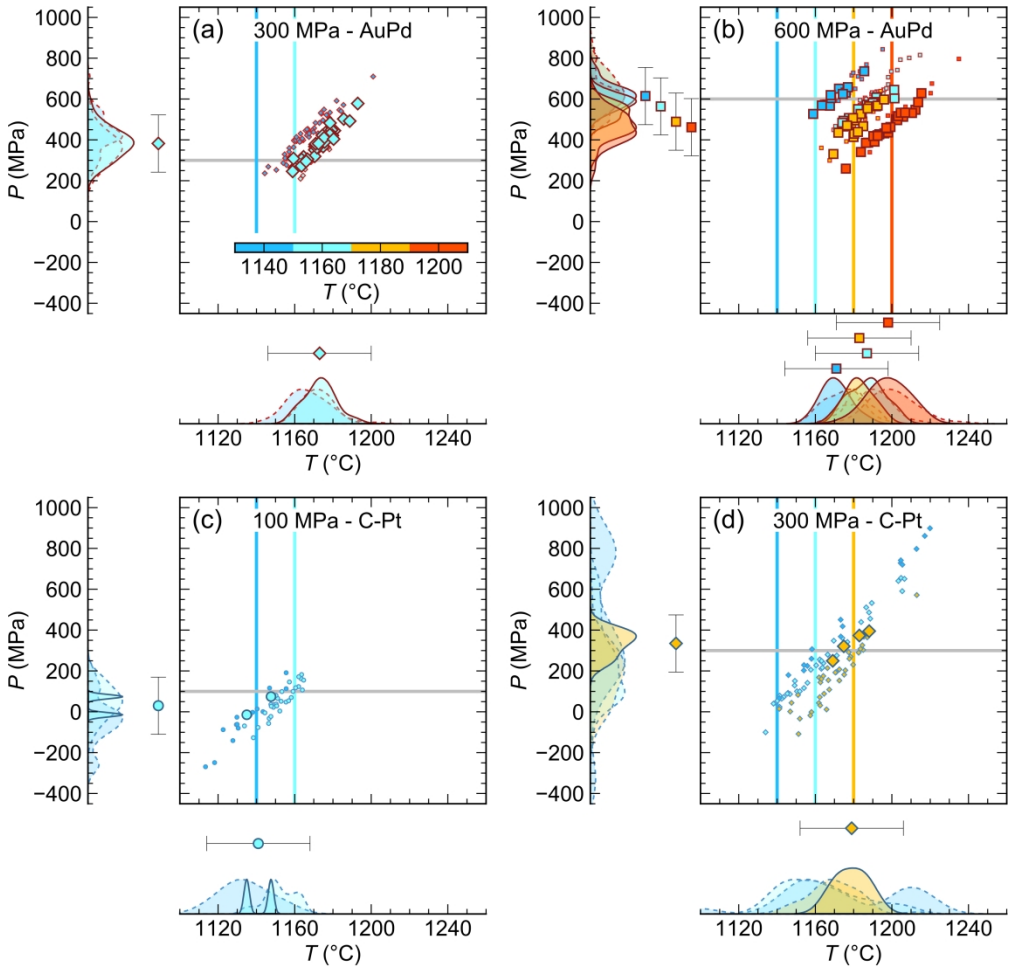
(a) 300 MPa - AuPd
(b) 600 MPa - AuPd
(c) 100 MPa - C-Pt
(d) 300 MPa - C-Pt
P (MPa)
T (°C)
1000
800
600
400
200
0
−200
−400
1120
1140
1160
1180
1200
1240

Fig. 13

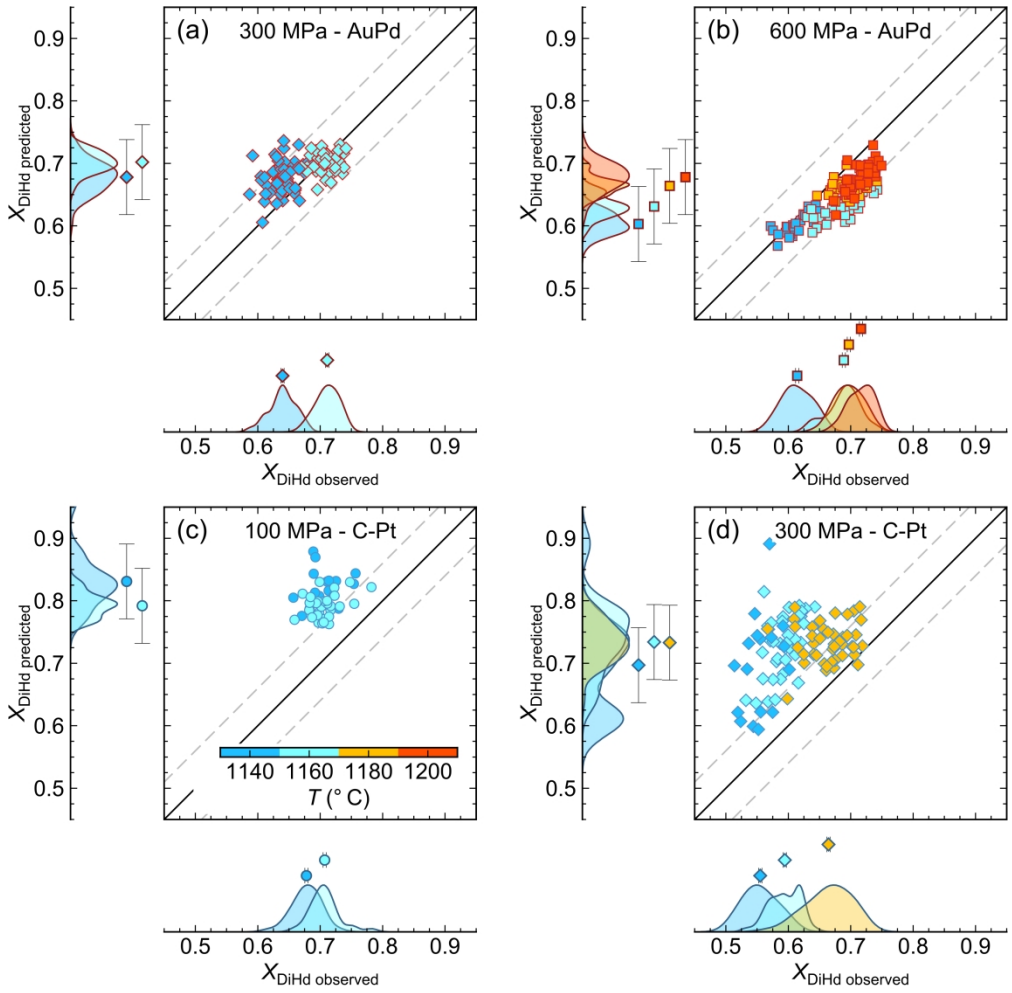
(a) 300 MPa - AuPd
(b) 600 MPa - AuPd
(c) 100 MPa - C-Pt
(d) 300 MPa - C-Pt
$X_{DiHd\ predicted}$
$X_{DiHd\ observed}$
0.5
0.6
0.7
0.8
0.9
1140 1160 1180 1200
T (° C)

Fig. 14

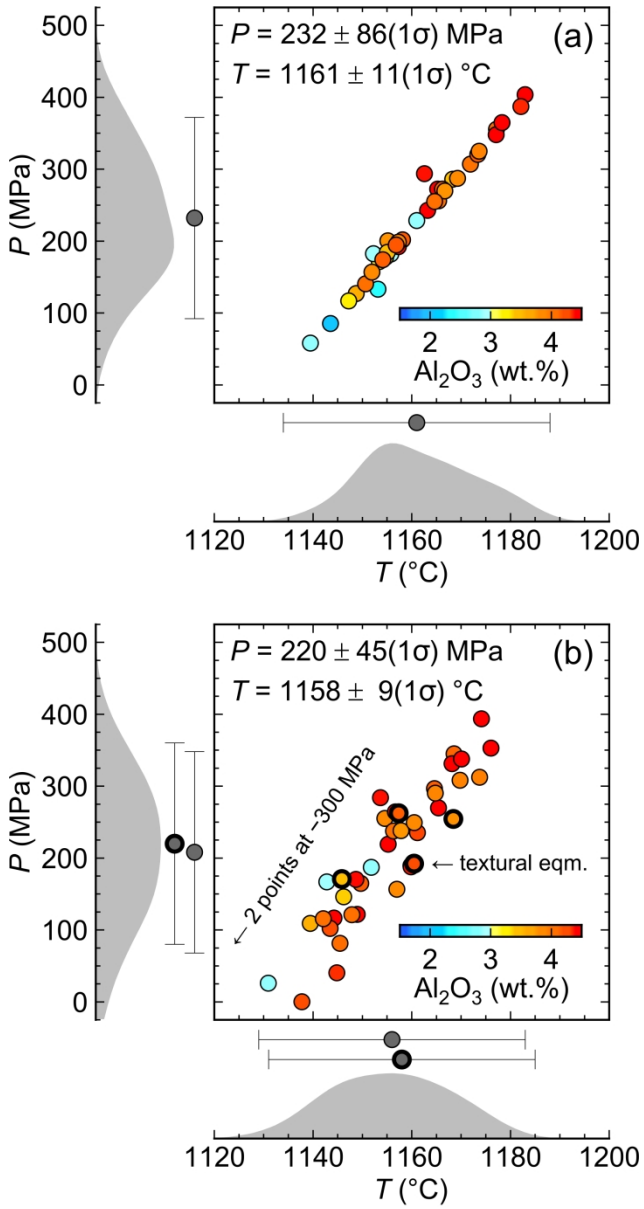
P = 232 ± 86(1σ) MPa
T = 1161 ± 11(1σ) °C
(a)
P (MPa)
500
400
300
200
100
0
2
3
4
Al2O3 (wt.%)
1120
1140
1160
1180
1200
T (°C)
P = 220 ± 45(1σ) MPa
T = 1158 ± 9(1σ) °C
(b)
← 2 points at ~300 MPa
← textural eqm.

Fig. 15

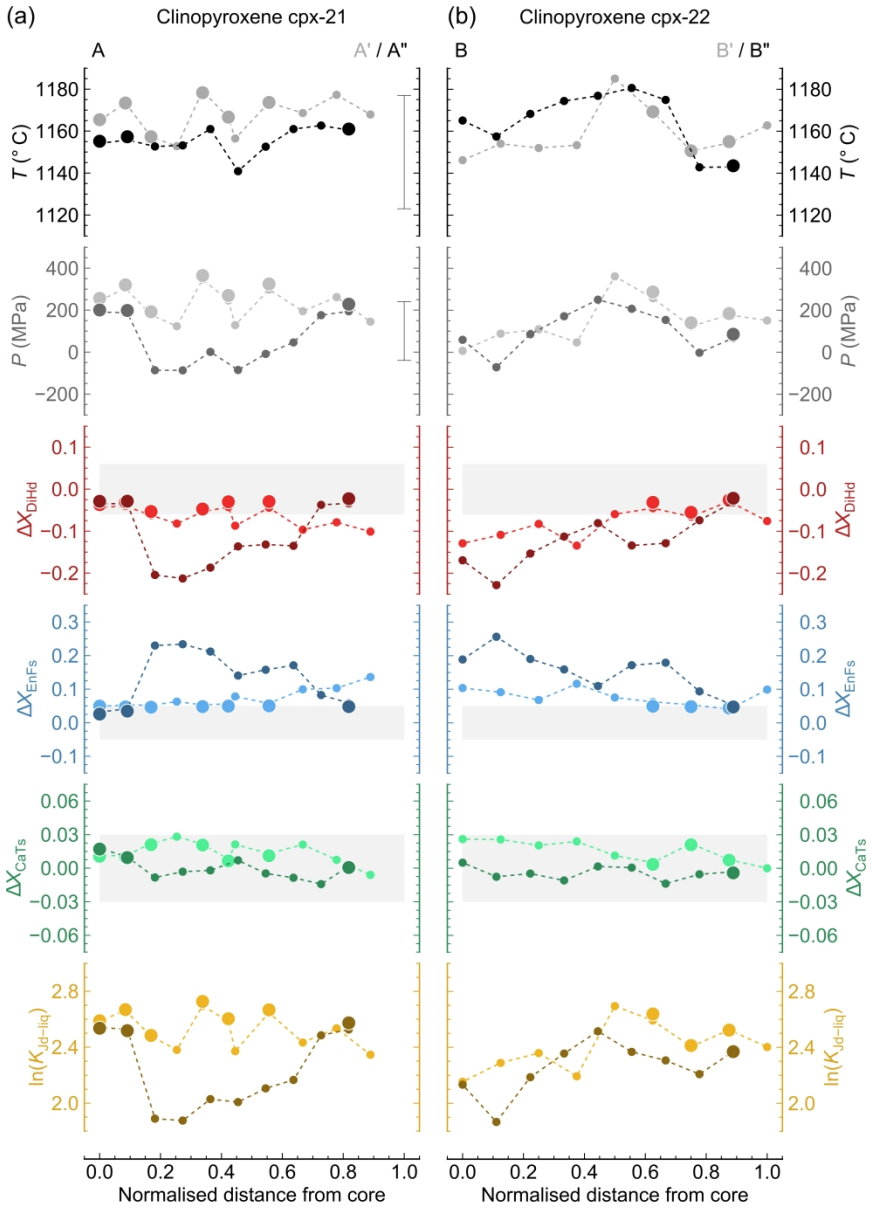
(a)
Clinopyroxene cpx-21
A
A' / A"
(b)
Clinopyroxene cpx-22
B
B' / B"
T (° C)
P (MPa)
ΔXDiHd
ΔXEnFs
ΔXCaTs
ln(KJd-liq)
Normalised distance from core
Normalised distance from core

Fig. 16